ISOTHERMAL COMPRESSIBILITY AND SPECIFIC HEAT OF HADRONIC MATTER FORMED IN HEAVY-ION COLLISIONS

Vassu Doomra

Roll No: MP16016

A dissertation submitted for the partial fulfilment
of MS degree in Physical Science

Under the guidance of

Dr. Satyajit Jena

April 2019

Indian Institute of Science Education and Research Mohali

Sector - 81, SAS Nagar, Mohali 140306, Punjab, India

Dedicated to friends and family

Certificate of Examination

This is to certify that the dissertation titled **"Isothermal Compressibility and Specific Heat of Hadronic Matter formed in Heavy-Ion Collisions"** submitted by **Vassu Doomra** (Reg. No. MP16016) for the partial fulfillment of MS degree program of the Institute, has been examined by the thesis committee duly appointed by the Institute. The committee finds the work done by the candidate satisfactory and recommends that the report be accepted.

Dr. Kinjalk Lochan | Dr. Anosh Joseph | Dr. Satyajit Jena (Supervisor)

Dated: 25.04.2019

Declaration

The work presented in this dissertation has been carried out by me under the guidance of Dr. Satyajit Jena at the Indian Institute of Science Education and Research Mohali.

This work has not been submitted in part or in full for a degree, a diploma, or a fellowship to any other university or institute. Whenever contributions of others are involved, every effort is made to indicate this clearly, with due acknowledgement of collaborative research and discussions. This thesis is a bonafide record of original work done by me and all sources listed within have been detailed in the bibliography.

Vassu Doomra
(Candidate)

Dated: April 25, 2019

In my capacity as the supervisor of the candidate's project work, I certify that the above statements by the candidate are true to the best of my knowledge.

Dr. Satyajit Jena
(Supervisor)

Acknowledgement

First and foremost, I would like to thank my thesis supervisor Dr. Satyajit Jena, to give me this valuable opportunity to do this wonderful project. Without his help and supervision, this thesis would have never been possible. The discussions that I had with him has enhanced my capabilities as a researcher. I would like to show my gratitude to Dr. Kinjalk Lochan and Dr. Anosh Joseph for their guidance and valuable inputs.

I would also like to thank my family for their constant emotional support during my degree. I am thankful to and fortunate enough to get valuable comment suggestions on my thesis from my colleagues here at IISER Mohali, India which greatly helped me to improve the quality of my thesis. Thanks especially to my friends and office mates Rohit Gupta, Vinay Gaba, Debjit Basu, Gargi Lather, Neha Nanda, Paras Koundal, Ojaswi Gupta, Nilotpal Kakati and Dr. Kirandeep Kaur, for the good company and chat, both work and non-work related, inside and outside the office.

Vassu Doomra

MP16016

IISER Mohali.

Out of the night that covers me,
Black as the pit from pole to pole,
I thank whatever gods may be
For my unconquerable soul.
In the fell clutch of circumstance
I have not winced nor cried aloud.
Under the bludgeonings of chance
My head is bloody, but unbowed.
Beyond this place of wrath and tears
Looms but the Horror of the shade,
And yet the menace of the years
Finds, and shall find me, unafraid.
It matters not how strait the gate,
How charged with punishments the scroll,
I am the master of my fate:
I am the captain of my soul.

William Ernest Henley

List of Figures

List of Tables

Contents

Abstract

According to big-bang theory, at the earliest of its expansion, the universe existed as Quark-Gluon-Plasma (QGP). As it cooled down, the deconfinement-confinement phase transition occurred, and hadrons were formed. A study of this phase transition can lead us to understand the early stages of universe formation. The transformation of matter at high enough energies, from nucleons to constituent quarks and gluons had been very fascinating and equally very challenging.

In this thesis, we intend to study ultra-relativistic heavy-ion collisions by using fluctuations of charged particle multiplicity and temperature. The study of event-by-event fluctuations of temperature and charged particle multiplicity will give an approximation of the specific heat and isothermal compressibility of the system respectively. A novel method has also been proposed for the specific heat calculation based on the lattice QCD (Quantum Chromodynamics) simulation results on the initial energy density in heavy-ion collisions. Together these two observables can predict something about the critical point in the QCD phase diagram. The temperature parameter is obtained from the transverse momentum distribution of the outgoing particles. Several models are studied for obtaining the best approximation to the experimental data on transverse momentum of identified particles from $Pb + Pb$ collisions at $\sqrt{s_{NN}}$ = 2.76 TeV. Charged particle multiplicity distributions are studied for $Au + Au$ collisions at $\sqrt{s_{NN}}$ = 200 GeV and the variation of isothermal compressibility is shown over a temperature range of 150 MeV to 250 MeV.

Chapter 1

Introduction

1.1 Building blocks of elementary particles

The current answer to the question, what the world is made of, is shown in Table 1.1. For many decades, protons, neutrons, and electrons were thought to be as the fundamental building blocks of matter until inelastic electron-proton scattering experiments were performed which showed that protons have a substructure comprising of particles called quarks [HM08]. Further experiments demonstrated that neutrons too have a substructure also comprising of quarks. Proton is made up of two up (u) and one down (d) quark whereas a neutron is comprised of two down and one up quark. The interactions among the quarks occur via the exchange of gluons. The force existing between the quarks is called **color force**. Quarks and gluons are collectively known as **partons**. Since quarks make up protons and neutrons (collectively called nucleons) and we also know that a strong nuclear force exists between the nucleons which hold them together within the nucleus, we can say that the color force is the origin of strong nuclear force.

However, there is a very crucial distinction between these two forces. Strong nuclear force is a short range force i.e. the strength of the force falls very rapidly with increasing distance between the nucleons. On the other hand, the strength of color force increases with the distance between the quarks. This behaviour of color force, known as **asymptotic freedom**, is discussed in the next section.

There are six quark flavors: u (up), d (down), s (strange), c (charm), t (top), b (bottom) and each quark may exist in three equivalent states differing in values of the new quantum number, termed as color.

Table 1.1: Building blocks of elementary particles and their electric charges

	Name	Electric Charge
Quarks	u (up)	2/3
	d (down)	-1/3
Leptons	electron	-1
	neutrino	0
Gauge Bosons	γ (photon)	0
	$W^{\pm}$, Z (weak bosons)	$\pm$1,0
	g_i (i =1,2,...8 gluons)	0

What is color quantum number?

Pauli exclusion principle forbids two identical fermions to occupy the same quantum state. However, making up hadrons from quarks, possessing spin 1/2, will lead to a contradiction to the exclusion principle, for example, a proton contains two up quarks and Ω^- particle is made of three strange quarks. The existence of such particles indicates that there must exist some another quantum number (in addition to spin) and since a maximum of three quark bound states exist in nature (baryons); this new quantum number must have three values. In 1965 three physicists Bogolubov, Struminsky and Tavkhelidze introduced the concept of color quantum number with colored quarks existing in three states, *green (G), red (R)* and *blue (B)*.

Since quarks are electrically charged, they will also interact by photon exchange, i.e., via electromagnetic interactions. However, we are familiar with the fact that electromagnetic interactions bind positronium, the bound state of an electron and its antiparticle positron, it is clear that electromagnetic interactions cannot bind quarks into hadrons. Considering the example of Δ^{++} particle, containing three u quarks, there must exist a "*strong*" force that will overrule the electromagnetic repulsion between u quarks and bind these quarks together to form Δ^{++} particle. In fact, a *color* charge endows the quarks with a new color field making this strong binding possible. As indicated earlier, gluons are the quanta of this color field. Gluon itself is a colored object: in fact, it is a bicolored object (color +

anticolor). Since there are three color states; R, G, B, and corresponding three anticolor states; antigreen ($\bar{G}$), antired ($\bar{R}$), antiblue ($\bar{B}$), we can have nine bicolored states: R$\bar{G}$, R$\bar{R}$, R$\bar{B}$, G$\bar{R}$, G$\bar{B}$, G$\bar{G}$, B$\bar{R}$, B$\bar{B}$, B$\bar{G}$. One of these nine combinations R$\bar{R}$+G$\bar{G}$+B$\bar{B}$ is a color singlet state which does not have any net color charge and thus cannot assume the job of a gluon carrying color from one quark to another.

The theory of strong interactions between quarks and gluons is known as Quantum Chromodynamics (QCD). It is a theory like electromagnetism but with eight gluons instead of a single photon. There are other important distinctions between the two theories:

- Photons are neutral particles, they do not carry any electric charge, but gluons are colored objects.
- The coulomb interactions between electric charges vary inversely as the distance between the charges whereas, as pointed out earlier, the color force strength increases with the distance between quarks.

1.2 Asymptotic Freedom

At short distances, the color force between the quarks is feeble. However, as the distance between the quarks increases, the force grows stronger. This is because of the ability of the gluons to create more gluons. Thus, if a quark starts to move apart from another quark after being hit by an energetic particle, the gluons will utilize this energy to produce more gluons. More the number of gluons exchanged between quarks, stronger will be the force. At some point, the force will become so strong that an additional quark-antiquark pair production energy will be reached before the quarks can be separated. This is why quarks can never be isolated and this is known as *color confinement*.

This behaviour of color force is taken into account in the QCD theory by defining a "*running*" coupling constant.

$$\alpha_s(Q^2) = \frac{12\pi}{(33 - 2n_f)log\frac{Q^2}{\Lambda^2}} \tag{1.1}$$

where n_f is the number of quarks active in pair production (upto 6), the quantity Λ is known as the QCD scale and is nearly equal to 0.2 GeV, Q is the momentum transfer between the quarks or the momentum carried by the gluons. Figure 1.1 shows the variation of α_s as a function of Q^2.

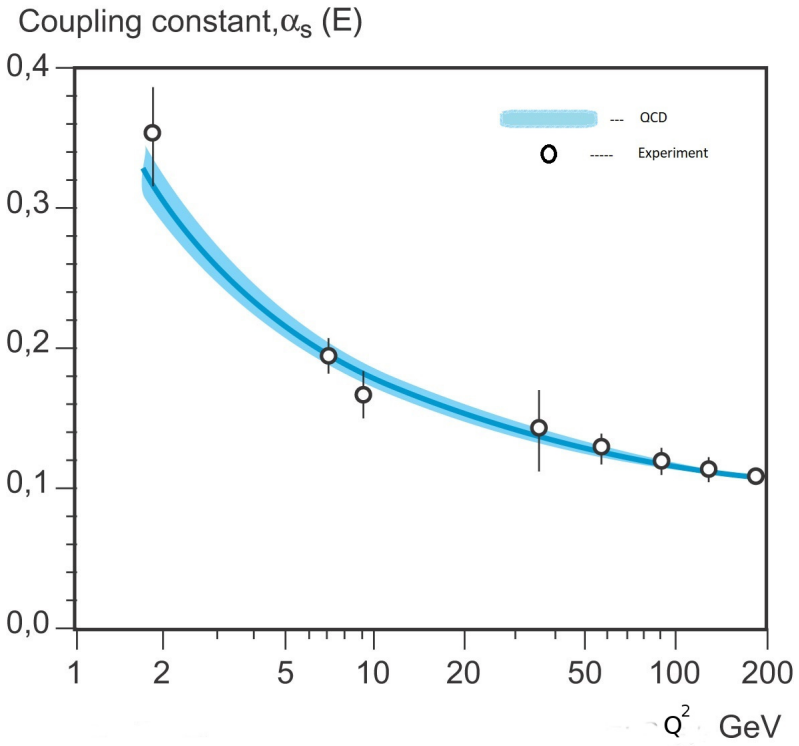

Figure 1.1: The running coupling constant, α_s, as a function of Q^2 (Image Source: Nobelprize.org)

Chapter 2

Quark-Gluon-Plasma and The Early Universe

For a few millionths of a second after the big-bang, the universe was filled with an extremely hot and dense soup of quarks and gluons known as the QGP. At such high temperatures, due to asymptotic freedom, even the strongly interacting particles, quarks and gluons, would interact very weakly. As the universe cooled down, the quarks and gluons hadronize resulting in the formation of baryonic matter that we see today.
The Relativistic Heavy-Ion Collider (RHIC) at Brookhaven National Laboratory (BNL) and Large Hadron Collider (LHC) at CERN are designed to recreate conditions similar to those of the microsecond old universe.

2.1 Conceptual Basis of the formation of Quark-Gluon-Plasma

[Cha14] At extremely high densities or temperatures, the notion of hadronic matter seems to lose its meaning. An increase in the energy density/temperature of the system (nucleus) leads to the production of an ever increasing number of low mass hadrons (mostly pions) which further results in a system of mutually interpenetrating hadrons.
Such a system of mutually interpenetrating hadrons is best considered as Quark matter rather than made of hadrons. Thus, at low energy densities/temperatures, the quarks are confined within the hadrons whereas at extreme conditions of energy densities/temperatures

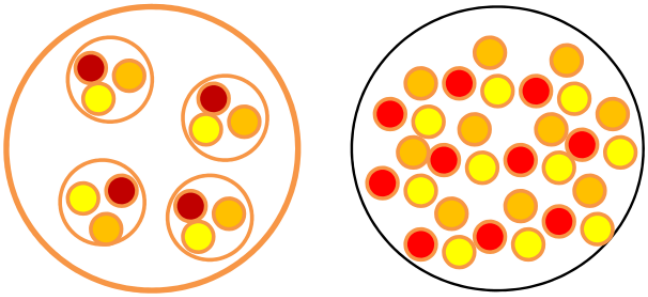

Figure 2.1: The figure on the left shows a nucleus at low energy density/temperature and the figure on the right shows the same system at extreme conditions of energy density/temperature (Image Source: [Cha14])

the quarks are in the deconfined state, as depicted in Figure 2.1. Hence, we can think of a confinement-deconfinement phase transition. An important point to note here is that it is not a phase transition in the thermodynamic sense (i.e., the derivatives of Gibbs free energy do not possess any discontinuity at the transition temperature), instead it is a gradual cross over from deconfinement to confinement or vice-versa.

In the deconfined state, the quarks are free to move over the nuclear volume rather than over the nucleonic volume. The deconfinement mechanism can be explained by the screening of color charge which is similar to Mott transition in atomic physics.

In matter, that is dense enough, the long-range coulomb potential which binds electrons and ions together in an electrically neutral atom, effectively becomes short range due to screening from other charges. Because of this screening, the ions can no longer bind the electrons and thus the insulating matter becomes conducting matter. Similarly in quark matter, quarks cannot be bound into a hadron due to the screening of color potential.

Note: There is an important difference between the QCD and the QED potentials.

$$\begin{aligned} V_{QED} &= -e^2/r \\ V_{QED} &= -\alpha/r + \sigma r \end{aligned} \tag{2.1}$$

However, we are concerned with the behaviour of these potentials at very high density or at very short distances. The difference between these potentials at large distances is of no significance then. Moreover, as a result of asymptotic freedom, at very short distances the coupling strength between the quarks is very weak which further enhances the deconfinement.

2.2 Heavy-Ion collisions

As mentioned above, with the advent of RHIC and LHC, it has become possible to study the QGP. These powerful particle accelerators make head-on collisions between massive ions, such as gold and lead nuclei, for this purpose. In these heavy-ion collisions, the hundreds of protons and neutrons in two such nuclei smash into one another at ultra-relativistic energies leading to the formation of a fireball in which everything melts into a *quark-gluon-plasma*. A relativistic nucleus-nucleus collision passes through different stages which are described below:

- **Pre-equilibrium Stage:** There is a pre-equilibrium stage before the formation of QGP. A successful picture of this initial stage was proposed by Bjorken. According to this picture, the production of particles in heavy-ion collisions is due to the excitation of vacuum caused by the collision of two beams of partons with subsequent production of virtual quanta. It takes a certain proper time T for these quanta to be de-excited to real quarks and gluons. The state of matter for $0 < \mathrm{t} < \mathrm{T}$ is said to be in the pre-equilibrium stage.

- **Expansion stage and Hadronization:** The collisions among the constituents of the fireball (QGP) establish a local thermal equilibrium state. In this state, the system has a thermal pressure against the outside vacuum. Because of this pressure gradient, the system evolves. As the system expands, the energy density/temperature decreases. Below a critical energy density $\epsilon_{cr} \approx 1GeV/fm^3$ or critical temperature $T_{cr} \approx 200$ MeV the QCD phase transition will occur and partons will transform to hadrons. This stage is known as hadronization stage.

- **Freeze-out:** Finally all the partons will be transformed into hadrons. The collisions among the hadrons will maintain a local equilibrium and the system will further expand and cool down. A stage will arrive when the inelastic collisions among the hadrons, in which the hadrons change identity, will become very infrequent. This stage is known as **chemical freeze-out**. The abundances of various hadron species will remain fixed after this stage. But hadrons can still collide elastically, that can still maintain a local equilibrium. The elastic collisions among the hadrons can change the final momentum distribution of the particles. But with further expansion, even the elastic collisions will become very infrequent and a local equilibrium could no

longer be maintained. The hadrons decouple or freeze-out. It is known as **kinetic freeze-out**.

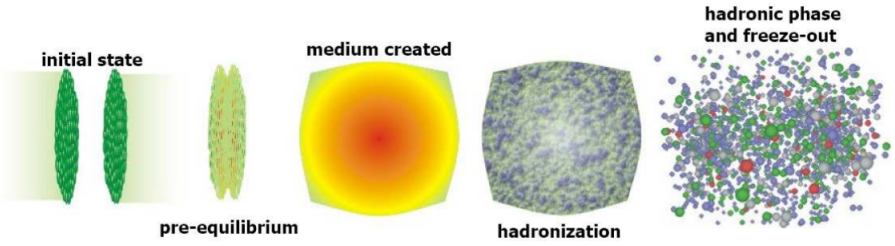

Figure 2.2: Schematic view of the space-time evolution of a nuclear collision (Image Source: [Cha14])

2.3 QCD Phase Diagram: Motivation for this study

Without going into the details of this phase diagram, shown in Figure 2.3, let us consider some of its important aspects:

- The y-axis is the temperature T in GeV and the x-axis represents the baryon chemical potential μ_B. The quantity μ_B is related to matter-antimatter asymmetry. A value of μ_B = 0 corresponds to a perfect matter-antimatter balance as it is expected in the microsecond old universe.

- Several models and lattice QCD simulations predict that at low T and high μ_B, First order phase transition occurs between the hadronic phase and the QGP phase and by increasing temperature and decreasing μ_B, a certain point is reached where the first order phase transition ends (blue line followed by the red point in the diagram). At high T and very low μ_B, the transition is just a cross over.

- The phase transition at the *critical point* is expected to be of the second-order.

- For a second-order phase transition, the second order derivatives of Gibbs function possesses a singularity at the transition temperature. The second order derivatives of Gibbs function with respect to pressure and temperature are directly related to specific heat and isothermal compressibility of the system respectively. Thus a determination of these two quantities in heavy-ion collisions would affirm the existence of

the predicted critical point and would also tell us something about its location on the phase diagram.

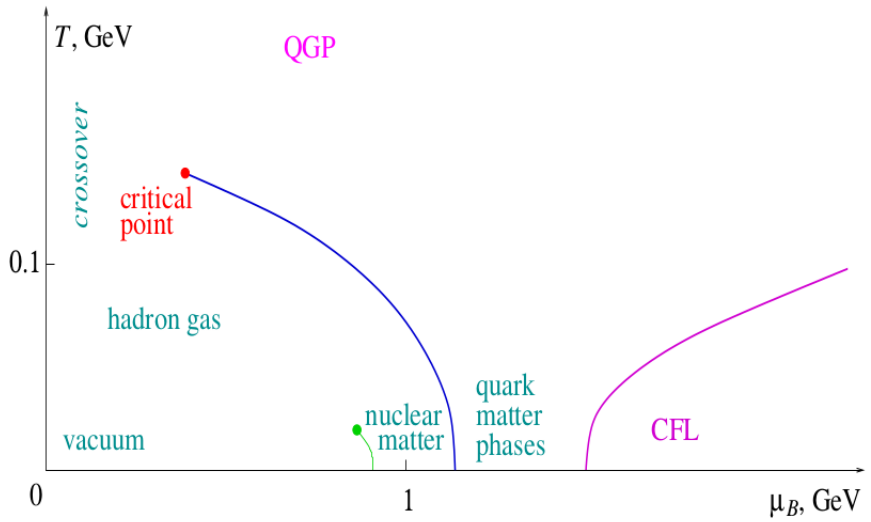

Figure 2.3: Schematic illustration of the QCD phase diagram in the T-μ_B plane (Image Source: [Ste06])

2.4 Signatures of QGP

In the final stage of heavy-ion collisions, the detector detects some thousands of particles produced in the collision. The deconfined medium of quarks and gluons exist for an extremely short duration. It is extremely difficult to directly detect QGP in this short lifetime. However, the various particles produced in the collision might prove to be useful as signatures of QGP. There may be no unique signal which will lead to the identification of QGP. Instead, a number of different signals come out from the medium which may be treated as QGP signatures. An account of some of these signatures is given below:

2.4.1 Elliptic Flow

In the case of non-zero impact parameter collisions, the overlap region of two nuclei is called the reaction zone. The initial reaction zone possesses azimuthal anisotropy. Multiple collisions between the constituent particles turn this spatial asymmetry into the momentum anisotropy of the produced particles. Mathematically, the observed momentum anisotropy

is defined as the Fourier expansion of Lorentz invariant differential yield in the angle ϕ given by:

$$E\frac{d^3N}{d^3p} = \frac{1}{2\pi}\frac{dN}{p_T dp_T dy}\left[1 + \sum_{n=1}^{\infty} 2v_n cosn\phi\right] \tag{2.2}$$

where ϕ is the azimuthal angle of the detected particle and v_n are called the flow coefficients. v_1 represents directed flow, v_2 is called elliptic flow, v_3 signifies triangular flow and so on. The second flow coefficient, elliptic flow, has been extensively studied in LHC and RHIC energy collisions and is considered as a direct signal of the formation of QGP. Elliptic flow measures the momentum anisotropy. As pointed out earlier, in non-zero impact parameter collisions, the initial participant zone is spatially anisotropic. If a thermalized medium is produced in the collision of nuclei, then this system will expand against the outside vacuum due to the pressure gradient. It is easy to see that the pressure gradient along the minor axis will be more than that along the major axis. Consequently, the rate of expansion will be more along the minor axis. As a result, particles tend to have a large collective flow in the direction of minor axis resulting in anisotropy in the momentum distribution of the partons. The more frequent the rescattering of the partons more is the resultant momentum anisotropy.

With subsequent expansion, the momentum anisotropy will cease to grow and will saturate when the reaction zone acquires azimuthal symmetry. Thus, it is easy to see that elliptic flow is a self-quenching phenomenon.

2.4.2 Jet Quenching

In ultra-relativistic heavy-ion collisions, the partons involved in the collisions are violently accelerated. The accelerated color charges emit QCD radiation in the form of gluons just like accelerated electric charges emit electromagnetic radiation in the form of photons. Photons are not electrically charged but gluons are color charged. Hence gluons can further emit more gluons or a gluon can decay into a quark-antiquark pair, thus leading to **parton showers**.

Jets are formed when a parton from a nucleus or nucleon scatters off of a parton from another nucleus or nucleon. After the scattering, the partons form parton showers which then hadronizes leading to a collimated spray of hadrons.

Now, if a hot and dense QGP medium is produced in nucleus-nucleus (AA) collision, then a jet created in early collision will propagate through this medium. Due to interaction with the medium, the jet particles will dissipate some energy while propagating through the medium. Usually, in experiments, the transverse momentum distribution of the particles produced in heavy-ion collisions is studied. The energy loss by the jet particles will result in a suppression of the high-p_t particles and is commonly known as *jet quenching*. Mathematically, jet quenching is measured through a quantity defined as *Nuclear Modification Factor (R_{AA})*, given by

$$R_{AA} = \frac{\frac{dN_{AA}}{d^2p_T dy}}{T_{AA}\frac{d\sigma_{AA}}{d^2p_T dy}} \tag{2.3}$$

The numerator is the single particle transverse momentum distribution of a jet parton produced in AA collision and travelling through the hot and dense QGP medium. The denominator shows single particle distribution of the same species of jet parton produced in pp collision multiplied by nuclear thickness function T_{AA} which is a proton to nucleus scaling factor (if AA collision is an incoherent superposition of pp collision) and is a function of impact parameter b. A value of R_{AA} equals to 1 indicates that no jet quenching has taken place. However if the ratio tends to be less than 1, it would mean that jet suppression has taken place in the medium and this would serve as a signature for QGP.

2.4.3 Net Charge Fluctuations

In the grand canonical ensemble formalism, for a system of classical ideal gas, net charge fluctuations are proportional to the square of electric charge which takes up distinct values for the QGP and hadronic phases. While the unit of charge in the hadronic phase is 1, in the QGP phase, it is 1/3. This may result in the fluctuation in net charge to vary with the change of phase, with the net charge remaining unaffected.

We can write the fluctuations in net charge as

$$\langle \delta Q^2 \rangle = q^2 \langle (\delta N_+ - \delta N_-)^2 \rangle \tag{2.4}$$

where q is the charge of the particles in the system, N_+ is the number of positively charged particles and N_- is the number of negatively charged particles in the system.

Using thermal distributions and disregarding correlations, we get

$$\langle \delta Q^2 \rangle = q^2 (\langle \delta N_+^2 \rangle + \langle \delta N_-^2 \rangle) \tag{2.5}$$

In the limit of very high temperature, both Fermi-Dirac and Bose-Einstein statistics reduce to the classical Maxwell-Boltzmann statistics. Moreover, at extremely high temperatures / energy densities, due to asymptotic freedom, quark interactions are very weak and we can approximate the hot and dense medium produced in heavy-ion collisions as a classical ideal gas.

For the case of a classical ideal gas in grand canonical ensemble, we have [Appendix A]

$$\langle N^2 \rangle - \langle N \rangle^2 = \langle N \rangle \tag{2.6}$$

Using this result and equation (2.5)

$$\langle \delta Q^2 \rangle = q^2(\langle N_+ \rangle + \langle N_- \rangle) \tag{2.7}$$

$$\langle \delta Q^2 \rangle = q^2 \langle N \rangle \tag{2.8}$$

where N = $N_+ + N_-$ is the total number of charged particles.

Using this relation and the principle outlined above, the measurement of net charge fluctuations can serve as a definite measure for the formation of QGP in heavy-ion collisions.

2.5 Kinematic Quantities

In dealing with the experimental data on high-energy collisions, one frequently encounters some kinematic variables. These include *collision centrality*, *rapidity* and *pseudorapidity*, described below:

2.5.1 Collision Centrality

The large accelerators like LHC and RHIC collide bunch of particles (nuclei) coming in from opposite directions. When one such particle from one beam scatters off of another particle in the other beam, this is what we define as one **event**.

A significant quantity characterizing any type of collision is the impact parameter (b). Small b collisions are called central whereas large impact parameter collisions are called peripheral. The impact parameter of each event varies during the collision. This variation of impact parameter is called **centrality**. For example, 0-5$\%$ centrality covers the impact parameter range from 0 to 3.50 fm (for $Pb + Pb$ collisions at $\sqrt{s_{NN}}$ = 2.76 TeV) [A$^+$13b]. The collection of all possible impact parameters is called a **minimum bias** sample.

However, the impact parameter is not the only way of characterizing the collision centrality. Centrality can also be defined in terms of the number of participating nucleons (N_{part}), a nucleon that has undergone at least one inelastic collision, or in terms of the binary nucleon collision number. These two parameters, however, have one to one correspondence with the impact parameter which can be estimated using a Glauber Model [A$^+$13b].

2.5.2 Rapidity

The rapidity of a particle is defined as

$$y = \frac{1}{2} ln \frac{E + p_z c}{E - p_z c} \tag{2.9}$$

where E is the total energy of the particle and p_z is it's longitudinal momentum. Conventionally the z-direction is taken as the beam axis.

How is rapidity useful?

Suppose a particle, in a collision, is predominantly produced along the beam direction say the +z direction. In that case $E \simeq p_z c$, so that $y \to \infty$. If the particle moved along the -z direction, then $y \to -\infty$. Consider now the particle being produced in a direction perpendicular to the beam axis, so that p_z = 0 and $y \to 0$. Thus we see that the rapidity of a particle is somehow related to the angle at which the particle is produced with respect to the beam direction.

There are also some other ways of writing the rapidity which are described below:

$$y = \frac{1}{2} ln \frac{E + p_z c}{E - p_z c} = ln \sqrt{\frac{E + p_z c}{E - p_z c}} \tag{2.10}$$

$$\begin{aligned} y = ln \sqrt{\frac{E + p_z c}{E - p_z c}} &= ln \frac{E + p_z c}{\sqrt{E + p_z c}\sqrt{E - p_z c}} \\ &= ln\Big(\frac{E + p_z c}{\sqrt{E^2 - p_z^2 c^2}}\Big) \end{aligned} \tag{2.11}$$

Using the definition of transverse mass, $M_T^2 c^4 = p_x^2 c^2 + p_y^2 c^2 + M^2 c^4$, where M is the rest mass, we get

$$y = ln\Big(\frac{E + p_z c}{M_T c^2}\Big) \tag{2.12}$$

For yet another expression, we will use the identity $tanh\theta = e^{\theta} - e^{-\theta}/e^{\theta} + e^{-\theta}$

$$y = tanh^{-1}\Big(tanh\Big(ln\Big(\frac{E + p_z c}{M_T c^2}\Big)\Big)\Big) \tag{2.13}$$

$$y = tanh^{-1}\left(\frac{exp\Big(ln\Big(\frac{E+p_zc}{M_Tc^2}\Big)\Big) - exp\Big(-ln\Big(\frac{E+p_zc}{M_Tc^2}\Big)\Big)}{exp\Big(ln\Big(\frac{E+p_zc}{M_Tc^2}\Big)\Big) + exp\Big(-ln\Big(\frac{E+p_zc}{M_Tc^2}\Big)\Big)}\right) \tag{2.14}$$

$$y = tanh^{-1}\left(\frac{\frac{E+p_zc}{M_Tc^2} - \frac{M_Tc^2}{E+p_zc}}{\frac{E+p_zc}{M_Tc^2} + \frac{M_Tc^2}{E+p_zc}}\right) \tag{2.15}$$

Using simple algebra we finally get

$$y = tanh^{-1}\left(\frac{p_zc(E+p_zc)}{E(E+p_zc)}\right) \tag{2.16}$$

$$y = tanh^{-1}\Big(\frac{p_zc}{E}\Big) \tag{2.17}$$

Rapidity transformation under Lorentz Boosts parallel to the beam direction:

For this we first need to see how the components of 4-momentum transforms with respect to boosts along the z direction

$$\begin{aligned} E'/c &= \gamma(E/c - \beta p_z) \\ p'_x &= p_x \\ p'_y &= p_y \\ p'_z &= \gamma(p_z - \beta E/c) \end{aligned} \tag{2.18}$$

so that we get from equation (1.1)

$$y' = \frac{1}{2}ln\left(\frac{\gamma E/c - \beta\gamma p_z + \gamma p_z - \beta\gamma E/c}{\gamma E/c - \beta\gamma p_z - \gamma p_z + \beta\gamma E/c}\right) \tag{2.19}$$

$$y' = \frac{1}{2}ln\left(\frac{(E/c + p_z)(\gamma(1-\beta))}{(E/c + p_z)(\gamma(1+\beta))}\right) \tag{2.20}$$

$$y' = \frac{1}{2}ln\frac{E+p_zc}{E-p_zc} + ln\sqrt{\frac{1-\beta}{1+\beta}} \tag{2.21}$$

$$y' = y + ln\sqrt{\frac{1-\beta}{1+\beta}} \tag{2.22}$$

This expression can further be simplified

$$\begin{aligned} ln\sqrt{\frac{1-\beta}{1+\beta}} &= tanh^{-1}\Big(tanh\Big(ln\sqrt{\frac{1-\beta}{1+\beta}}\Big)\Big) \\ &= tanh^{-1}\left(\frac{\sqrt{\frac{1-\beta}{1+\beta}} - \sqrt{\frac{1+\beta}{1-\beta}}}{\sqrt{\frac{1-\beta}{1+\beta}} + \sqrt{\frac{1+\beta}{1-\beta}}}\right) \\ &= -tanh^{-1}\beta \end{aligned} \tag{2.23}$$

Thus we finally get from above equations

$$y' = y - tanh^{-1}\beta \tag{2.24}$$

Suppose there are two particles flying out of the collision region. Some observer measures their rapidities to be y_1 and y_2. Now if some other observer measures these rapidities from a different reference frame and get y_1' and y_2', then,

$$y_1' - y_2' = \left(y_1 - tanh^{-1}\beta - y_2 + tanh^{-1}\beta\right) = y_1 - y_2 \tag{2.25}$$

Thus the rapidity difference between two particles is invariant with respect to boosts along the beam direction. This is why rapidity is so important in experimental high-energy physics.

2.5.3 Pseudo-rapidity

For outgoing particles with very high p_z values, it can be challenging to measure the p_z value precisely because the beam pipe can be in the way of estimating it and hence the rapidity can be hard to measure for such particles. However, we can define a quantity that is nearly the same as rapidity but can be determined much easily than rapidity for highly relativistic particles. The quantity is called pseudo-rapidity (η).

Starting with the definition of rapidity

$$y = \frac{1}{2} ln \frac{E + p_z c}{E - p_z c} \tag{2.26}$$

$$y = \frac{1}{2} ln \left(\frac{(p^2c^2 + m^2c^4)^{1/2} + p_z c}{(p^2c^2 + m^2c^4)^{1/2} - p_z c} \right) \tag{2.27}$$

For a highly relativistic particle $pc << mc^2$

$$y = \frac{1}{2} ln \left(\frac{pc(1 + \frac{m^2c^4}{p^2c^2}) + p_z c}{pc(1 + \frac{m^2c^4}{p^2c^2}) - p_z c} \right) \tag{2.28}$$

$$y \simeq \frac{1}{2} ln \left(\frac{pc + p_z c + \frac{m^2c^4}{2pc} + \cdots}{pc - p_z c + \frac{m^2c^4}{2pc} + \cdots} \right) \tag{2.29}$$

$$y \simeq \frac{1}{2} ln \left(\frac{1 + \frac{p_z}{p} + \frac{m^2c^4}{2p^2c^2} + \cdots}{1 - \frac{p_z}{p} + \frac{m^2c^4}{2p^2c^2} + \cdots} \right) \tag{2.30}$$

Now $p_z/p = cos\theta$, where θ is the angle made by the particle trajectory with the beam pipe.

$$1 + \frac{p_z}{p} = 1 + cos\theta = 2cos^2\frac{\theta}{2} \tag{2.31}$$

$$1 - \frac{p_z}{p} = 1 - cos\theta = 2sin^2\frac{\theta}{2} \tag{2.32}$$

Substituting these back into equation (2.30) and neglecting the higher order terms we get

$$y \simeq -ln(tan\Big(\frac{\theta}{2}\Big)) \tag{2.33}$$

Thus we define pseudo-rapidity as

$$\eta = -ln(tan\Big(\frac{\theta}{2}\Big)) \tag{2.34}$$

Thus we see that the quantity η is directly related to the angle at which the particle is emitted with respect to the beam direction and hence is much easier to calculate.

Chapter 3

Charged Particle Multiplicity Distribution and Isothermal Compressibility

3.1 Introduction

The isothermal compressibility (k_T) describes the relative change in the volume of a system due to a change in the pressure at a constant temperature and is defined as

$$k_T = -\frac{1}{V}\frac{\delta V}{\delta P}\Big|_T \tag{3.1}$$

where V is the volume, T is the temperature, and P is the pressure of the system.

In the present work, the isothermal compressibility of hadronic matter formed in heavy-ion collisions is determined from the event-by-event fluctuations of charged particle multiplicities in the midrapidity region. The experimental data on charged particle multiplicity distributions at the RHIC have been used in combination with the HIJING event generator [WG91] studies, for volume calculation, to extract the values of k_T .

To obtain a relation between k_T and charged particle multiplicity fluctuations, we assume that heavy-ion collisions at ultra-relativistic energies can be considered as a thermal system in the grand canonical ensemble (GCE). In the GCE formalism, we can write the average number of particles as :

$$\langle N \rangle = \frac{1}{Z}\sum\nolimits_{states} N e^{-\beta(E-\mu N)} \tag{3.2}$$

from which we can obtain

$$\left(\frac{\partial\langle N\rangle}{\partial\mu}\right)_{V,T} = \frac{1}{Z}\sum\nolimits_{states}\beta N^2 e^{-\beta(E-\mu N)} - \frac{1}{Z^2}\left(\frac{\partial Z}{\partial\mu}\right)\sum\nolimits_{states} N e^{-\beta(E-\mu N)} \tag{3.3}$$

where

$$\left(\frac{\partial Z}{\partial\mu}\right) = \sum\nolimits_{states}\beta N e^{-\beta(E-\mu N)} = \beta Z\langle N\rangle \tag{3.4}$$

Using the above two equations we get the following equation

$$\left(\frac{\partial\langle N\rangle}{\partial\mu}\right)_{V,T} = \beta(\langle N^2\rangle - \langle N\rangle^2) \tag{3.5}$$

$$\left(\frac{\partial\langle N\rangle}{\partial\mu}\right)_{V,T} = \left(\frac{\partial\langle N\rangle}{\partial P}\right)_{V,T}\left(\frac{\partial P}{\partial\mu}\right)_{V,T} \tag{3.6}$$

We can define a quantity called specific volume which is the volume per particle as

$$v = \frac{V}{\langle N\rangle} \tag{3.7}$$

Using this definition of specific volume we can further write

$$\left(\frac{\partial\langle N\rangle}{\partial P}\right)_{V,T} = \left(\frac{\partial V/v}{\partial P}\right)_{V,T} = -\frac{V}{v^2}\left(\frac{\partial v}{\partial P}\right)_{V,T} \tag{3.8}$$

The Helmotz free energy (F) is defined as

$$F = E - TS - \mu N \tag{3.9}$$

where E is the internal energy, T is the temperature, S is the entropy, μ is the chemical potential of the system and N is the number of particles in the system. The differential of Helmotz free energy can be written as

$$dF = -pdV - SdT - Nd\mu \tag{3.10}$$

From this equation we get

$$\left(\frac{\partial P}{\partial\mu}\right)_{V,T} = \frac{N}{V} \tag{3.11}$$

Thus the final equation looks like

$$\left(\frac{\partial\langle N\rangle}{\partial\mu}\right)_{V,T} = -\frac{N\langle N^2\rangle}{V^2}\left(\frac{\partial v}{\partial P}\right)_{V,T} \tag{3.12}$$

$$\langle N^2\rangle - \langle N\rangle^2 = \frac{k_B T\langle N\rangle^2}{V}k_T \tag{3.13}$$

The charged particle multiplicity fluctuations, designated ω_{ch} , can generally be defined as:

$$\omega_{ch} = \frac{\langle N_{ch}^2 \rangle - \langle N_{ch} \rangle^2}{\langle N_{ch} \rangle} = \frac{\sigma_{ch}^2}{\mu_{ch}} \tag{3.14}$$

where N_{ch} is the charged particle multiplicity. The quantity ω_{ch} is also known as the scaled variance.

From equations (3.13) and (3.14) we obtain

$$\omega_{ch} = \frac{k_B T \langle N_{ch} \rangle}{V} k_T \tag{3.15}$$

It has been well established that the *Negative Binomial Distribution (NBD)* approximates well the experimental data on multiplicity distributions in heavy-ion collisions [B$^+$93], [Aea95]. So we will first discuss in detail about the negative binomial distribution.

3.2 Negative Binomial distribution

We begin with the definition of a *Bernoulli* trial. A Bernoulli trial is the one that can have only two outcomes, success or failure. A negative binomial distribution has the following properties:

- The Bernoulli trials are independent of each other.
- The probability for success, *p*, remains the same for all trials.
- The number of trials *n* should be finite.
- The events should be discrete.

There are two versions of a NBD.

In the first version, we count the number of the trials at which the r^{th} success occurs. With this version,

$$P(X_1 = x) = \binom{x-1}{r-1} p^r (1-p)^{x-r} \tag{3.16}$$

for integer x $\geq$ r. Here 0 $<$ p $<$ 1 and r $\geq$ 0.

The second version, the number of failures before the r^{th} success is counted. In this version,

$$P(X_1 = x) = \binom{x+r-1}{x} p^r (1-p)^x \tag{3.17}$$

for integer x $\geq$ 0.

Let us standardize on this second version for realizing two fundamental properties of a negative binomial distribution. The mean (μ) and variance (σ^2) of this distribution is given by

$$\mu = \frac{r(1-p)}{p} \tag{3.18}$$

$$\sigma^2 = \frac{r(1-p)^2}{p^2} = \mu + \frac{\mu^2}{r} \tag{3.19}$$

- A negative binomial distribution reduces to a **geometric** distribution in the limit of r $\rightarrow$ 1. Just as there are two versions of NBD, the geometric distribution also has two versions.

  In the first version, we determine the probability distribution of the number of trials, X, needed to get one success, so that

  $$P(X = k) = (1-p)^{k-1}p \tag{3.20}$$

  In the second version, we determine the probability distribution of the number Y = X - 1 of failures before the Ist success, so that

  $$P(Y = k) = (1-p)^{k}p \tag{3.21}$$

  It can easily be seen from the two definitions of NBD that for the particular case of r = 1, the NBD reduces to geometric distribution.

- In the limit of p $\rightarrow$ 1 and r $\rightarrow \infty$ as μ stays constant, P (X = x) reduces to $\frac{e^{\mu}\mu(x)}{x!}$, the probability distribution for a poisson distribution. This can easily be seen from equation (3.19). The poisson distribution requires the mean and variance to be equal which is true in this limit.

3.2.1 What's negative about a Negative Binomial Distribution?

This question will be automatically answered if we get to know the distinction between binomial and negative binomial distribution.

In the case of a Binomial distribution, the number of trials n is kept fixed and we determine the probability distribution of the number of successes in n trials. However, in the case of NBD, not the number of trials but the number of successes is kept fixed and we determine the probability distribution of the number of failures before the r^{th} success. Hence the

name, negative binomial distribution.

In the present analysis, we are using the following form of the Negative Binomial Distribution

$$P(n) = \frac{\Gamma(n + k_{NBD})}{\Gamma(n+1)\Gamma(k_{NBD})} \frac{(\mu_{ch}/k_{NBD})^n}{(1 + \mu_{ch}/k_{NBD})^{n+k_{NBD}}} \tag{3.22}$$

where P(n) is normalized to 1 over $0 \leq n \leq \infty$, μ_{ch} = $\langle N_{ch} \rangle$ = $\langle n \rangle$ and k_{NBD} is an additional parameter.

3.2.2 Mean and Variance of NBD

For the above NBD of an integer n, we have

$$\langle n \rangle = \mu_{ch} = \sum_{n=0}^{\infty} nP(n) \tag{3.23}$$

$$\langle n^2 \rangle = \sum_{n=0}^{\infty} n^2 P(n) \tag{3.24}$$

$$\langle n^2 \rangle = \sum_{n=0}^{\infty} n^2 \frac{\Gamma(n + k_{NBD})}{\Gamma(n+1)\Gamma(k_{NBD})} \frac{(\mu_{ch}/k_{NBD})^n}{(1 + \mu_{ch}/k_{NBD})^{n+k_{NBD}}} \tag{3.25}$$

$$\langle n^2 \rangle = \sum_{n=1}^{\infty} n^2 \frac{\Gamma(n + k_{NBD})}{\Gamma(n+1)\Gamma(k_{NBD})} \frac{(\mu_{ch}/k_{NBD})^n}{(1 + \mu_{ch}/k_{NBD})^{n+k_{NBD}}} \tag{3.26}$$

$$\langle n^2 \rangle = \sum_{n=0}^{\infty} (n+1)^2 \frac{\Gamma(n + k_{NBD} + 1)}{\Gamma(n+2)\Gamma(k_{NBD})} \frac{(\mu_{ch}/k_{NBD})^{n+1}}{(1 + \mu_{ch}/k_{NBD})^{1+n+k_{NBD}}} \tag{3.27}$$

$$\langle n^2 \rangle = \frac{(\mu_{ch}/k_{NBD})}{1 + \mu_{ch}/k_{NBD}} \sum_{n=0}^{\infty} (n+1)^2 \frac{\Gamma(n + k_{NBD} + 1)}{\Gamma(n+2)\Gamma(k_{NBD})} \frac{(\mu_{ch}/k_{NBD})^n}{(1 + \mu_{ch}/k_{NBD})^{n+k_{NBD}}} \tag{3.28}$$

$$\langle n^2 \rangle = \frac{(\mu_{ch}/k_{NBD})}{1 + \mu_{ch}/k_{NBD}} \sum_{n=0}^{\infty} (n+1)(n + k_{NBD}) P(n) \tag{3.29}$$

$$\langle n^2 \rangle = \frac{(\mu_{ch}/k_{NBD})}{1 + \mu_{ch}/k_{NBD}} \sum_{n=0}^{\infty} n^2 P(n) + k_{NBD} n P(n) + nP(n) + k_{NBD} P(n) \tag{3.30}$$

$$\langle n^2 \rangle = \frac{1}{1 + k_{NBD}/\mu_{ch}} \sum_{n=0}^{\infty} n^2 P(n) + k_{NBD} n P(n) + nP(n) + k_{NBD} P(n) \tag{3.31}$$

Using this expression together with the definitions of μ_{ch} and ω_{ch} we get

$$\langle n^2 \rangle = \mu_{ch}^2 + \mu_{ch} + \frac{\mu_{ch}^2}{k_{NBD}} \tag{3.32}$$

from which follows

$$\omega_{ch} = 1 + \frac{\mu_{ch}}{k_{NBD}} \tag{3.33}$$

From equation (3.33) we can see that the NBD converges to Poisson Distribution in the limit $k_{NBD} \to \infty$ and to Geometric distribution in the limit of $k_{NBD} \to 1$.

In the present work, charged particle multiplicity distribution data for $Au + Au$ collisions at $\sqrt{s_{NN}}$ = 200 GeV is being fitted with a NBD for various centralities. Using the fit parameters, the scaled variance or the multiplicity fluctuations are determined.

3.3 Charged Particle Multiplicity Distributions for $Au + Au$ collisions at $\sqrt{s_{NN}}$ = 200 GeV

Figure 3.1 shows the raw or uncorrected charged hadron multiplicity distributions in the range $0.2 < p_t < 2.0$ GeV for all centralities superimposed with fits to NBD (solid red lines) [A$^+$08].

As can be seen, the NBD describe the experimental data really well. The mean and variance of the distributions, as extracted from the NBD fits, are compiled in Table 3.1.

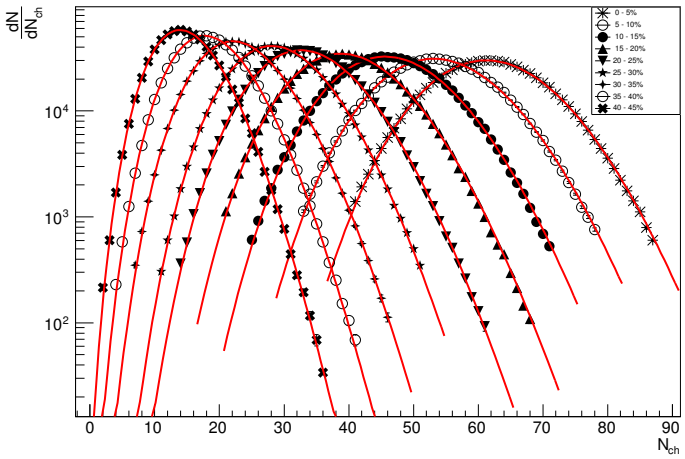

Figure 3.1: Uncorrected charged hadron multiplicity distributions over the range $0.2 < p_t < 2.0$ GeV/c for 200 GeV $Au + Au$ collisions. The solid lines represents the NBD fits to the data.

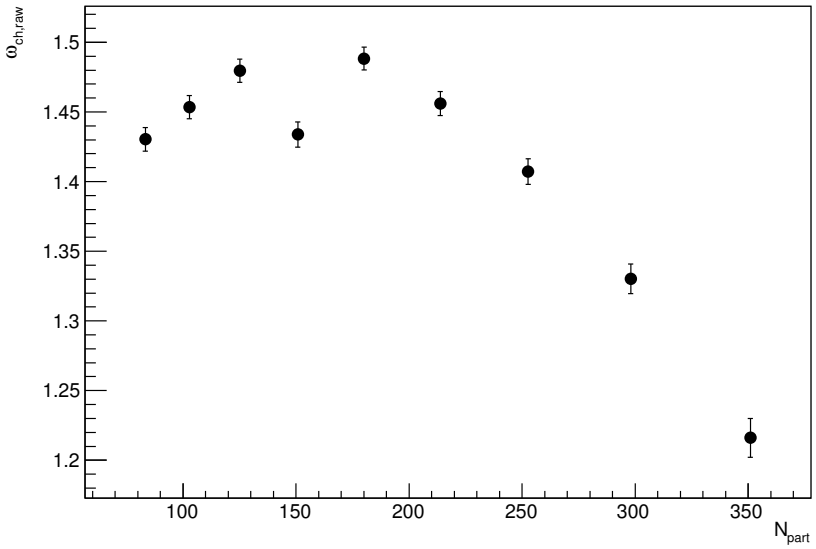

Figure 3.2: Raw or uncorrected multiplicity fluctuations, $\omega_{ch,raw}$, expressed as the scaled variance as a function of centrality for 200 GeV $Au + Au$ collisions in the range 0.2 $< p_t <$ 2.0 GeV/c.

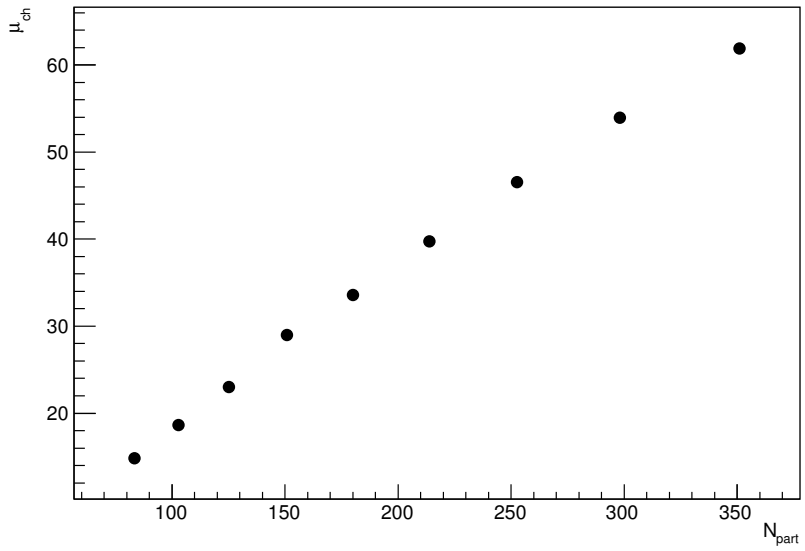

Figure 3.3: Variation of mean, extracted from the NBD fits, as a function of N_{part} for $Au + Au$ collisions over the range 0.2 $< p_t <$ 2.0 GeV/c.

The non-zero width of various centrality bins indicate that each centrality bin essentially selects a range of impact parameters. Because of this, a non-dynamical fluctuation component is introduced to the measured multiplicity fluctuations. Therefore, it becomes necessary to

Table 3.1: Tabulation of charged particle multiplicity data over the range $0.2 < p_t < 2.0$ GeV/c. The first five columns list the centrality, minimum and maximum values of impact parameter, number of participants and geometric correction factor f_{geo} respectively. μ_{ch} and k_{NBD} are extracted from the NBD fits. $\omega_{ch,dyn}$ represents the dynamical contribution to the multiplicity fluctuations.

Centrality	b_{min}	b_{max}	N_{part}	f_{geo}	μ_{ch}	k_{NBD}	$\omega_{ch,dyn}$
0-5	0	3.31	351	0.575	61.92 $\pm$0.0113	286.5 $\pm$3.291	1.124 $\pm$0.008
5-10	3.31	4.68	298.1	0.715	53.95 $\pm$0.011	163.4 $\pm$1.314	1.236 $\pm$0.007
10-15	4.68	5.73	252.7	0.785	46.53 $\pm$0.010	114.3 $\pm$0.756	1.320 $\pm$0.007
15-20	5.73	6.61	213.8	0.848	39.74 $\pm$0.0095	87.15 $\pm$0.516	1.387 $\pm$0.007
20-25	6.61	7.39	180.1	0.852	33.57 $\pm$0.0085	68.76 $\pm$0.378	1.415 $\pm$0.007
25-30	7.39	8.1	150.8	0.898	29.01 $\pm$0.0080	66.86 $\pm$0.42	1.390 $\pm$0.008
30-35	8.1	8.75	125.1	0.888	23.02 $\pm$0.0072	48.01 $\pm$0.267	1.426 $\pm$0.007
35-40	8.75	9.35	102.8	0.918	18.64 $\pm$0.0064	41.11 $\pm$0.236	1.416 $\pm$0.008
40-45	9.35	9.92	83.36	0.869	14.84 $\pm$0.0056	34.48 $\pm$0.2018	1.374 $\pm$0.007

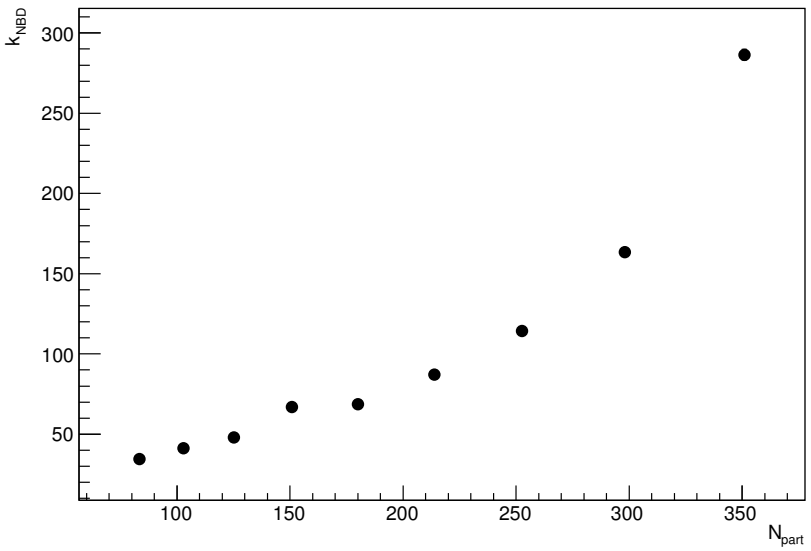

Figure 3.4: The parameter k_{NBD} extracted from the NBD fits as a function of the number of participating nucleons for $Au + Au$ (upper) collisions over the range $0.2 < p_t < 2.0$ GeV/c.

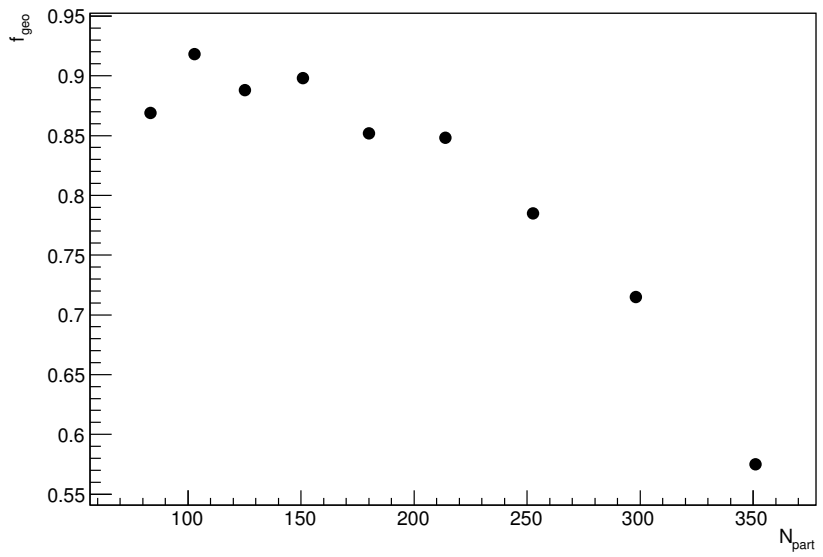

Figure 3.5: The factor f_{geo} calculated for various centralities using the HIJING event generator

calculate the extent of the geometry fluctuation component so that only the interesting dynamical fluctuations are left behind. In the present work, the HIJING event generator is employed for this estimate, because it reproduces well the mean multiplicity in heavy-ion collisions. The calculation is performed for each centrality class using the following procedure. First, HIJING is run with an impact parameter range corresponding to a given centrality class (which is known from the an improved Monte Carlo Glauber Model [LKd18]). Second, HIJING is run at a fixed impact parameter with a value equal to the mean of the impact parameter range in the first run. 10,000 HIJING events are processed for each centrality bin. The scaled variances for each centrality bin selection, $\omega_{Glauber}$ and ω_{fixed} , are calculated and the measured scaled variance is corrected as the fractional deviation from a scaled variance of 1.0 of a Poisson distribution as follows:

$$\omega_{ch,dyn} - 1 = \frac{\omega_{fixed} - 1}{\omega_{glauber} - 1}(\omega_{ch,raw} - 1) = f_{geo}(\omega_{ch,raw} - 1) \tag{3.34}$$

Using the procedure defined above we get the results shown in Figures 3.5 and 3.6. Figure 3.5 shows the f_{geo} calculated for various centralities of $Au + Au$ collisions at $\sqrt{s_{NN}}$ = 200 GeV using the HIJING event generator. Figure 3.6 shows the $\omega_{ch,dynamical}$ calculated using the f_{geo} factors.

A look at equation (3.15) tells us that in order to calculate k_T, we need information on volume as well as temperature of the system. For the purpose of volume calculation, we turn

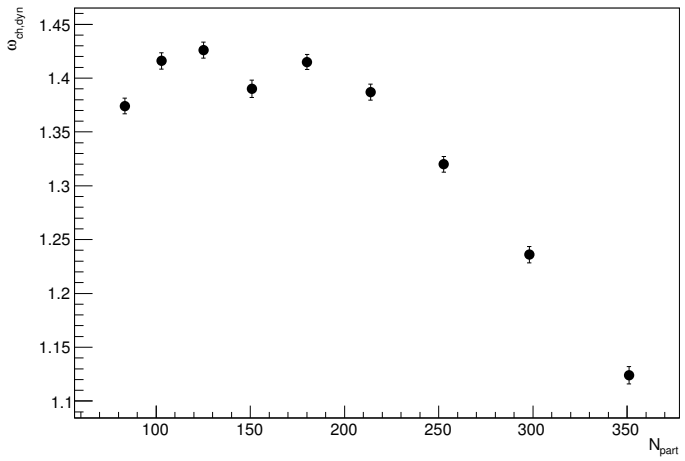

Figure 3.6: $\omega_{ch,dynamical}$ calculated using the f_{geo} factor for $Au + Au$ collisions at 200 GeV centre of mass energy

our attention to [BMKRS15].

Assuming a thermal medium of strongly interacting particles at temperature T and occupying a volume V, where, on an average, the strangeness S, electric charge Q and baryon number B is conserved, the fluctuations of the net charge N can be written as

$$\hat{\chi_N} = \frac{\chi_N}{T^2} = \frac{1}{VT^3}\sum_{n=1}^{|q|} n^2(\langle N_n\rangle + \langle N_{-n}\rangle) \tag{3.35}$$

where $|q|$ = (1,2,3) and $|q|$ = (1,2) for strangeness and electric charge respectively.

The above expression, for the correlation among different charges, gives

$$\chi_{\hat{NM}} = \frac{\chi_{NM}}{T^2} = \frac{1}{VT^3}\sum_{n=-q_N}^{q_N}\sum_{n=-q_M}^{q_M} nm\langle N_{n,m}\rangle \tag{3.36}$$

Using equations (3.35) and (3.36), the strangeness, net baryon number and charge-strangeness correlation susceptibilities can be expressed in terms of various particle yields as

$$\begin{aligned}\frac{\chi_S}{T^2} = \frac{1}{VT^3}[(\langle K^+\rangle + K^0\rangle + \langle\Lambda\rangle + \langle\Sigma^0\rangle + \langle\Sigma^+\rangle + \langle\Sigma^-\rangle + 4\langle\Xi^0\rangle + 4\langle\Xi^-\rangle \\ +9\langle\Omega^-\rangle) \ -(\Gamma_{\phi\to K^+} + \Gamma_{\phi\to K^-} + \Gamma_{\phi\to K^0} + \Gamma_{\phi\to \bar{K^0}})\phi\rangle]\end{aligned} \tag{3.37}$$

$$\begin{aligned}\frac{\chi_B}{T^2} = \frac{1}{VT^3}[\langle p\rangle + \langle N\rangle + \langle\Lambda\rangle + \langle\Sigma^0\rangle + \langle\Sigma^+\rangle + \langle\Sigma^-\rangle + \langle\Xi^0\rangle + \langle\Xi^-\rangle \\ +\langle\Omega^-\rangle + antiparticles]\end{aligned} \tag{3.38}$$

$$\begin{aligned}\frac{\chi_{QS}}{T^2} = \frac{1}{VT^3}[(\langle K^+\rangle + 2\langle\Xi^-\rangle + 3\langle\Omega^-\rangle) - (\Gamma_{\phi\to K^+} + \Gamma_{\phi\to K^-})\langle\phi\rangle \\ -(\Gamma_{K_0^*\to K^+} + \Gamma_{K_0^*\to K^-})\langle K_0^*\rangle]\end{aligned} \tag{3.39}$$

$\langle\rangle$ denotes the mean particle yield. The branching ratios, $\Gamma_{\phi\to K^0}$ = 0.342 $\pm$ 0.004, $\Gamma_{\phi\to K}$ = 0.489 $\pm$ 0.005 and $\Gamma_{K_0^*\to K^+}$ = 0.666 are from [O$^+$14]. Table 3.2 shows the results obtained for the three susceptibilities using HIJING event generator for $Au+Au$ collisions at $\sqrt{s_{NN}}$ = 200 GeV for various centrality classes. For each centrality, 10,000 HIJING events are used for the determination of the susceptibilities.

3.3.1 Volume Calculation from susceptibilities

The quantities $\frac{\chi_B}{T^2}$, $\frac{\chi_S}{T^2}$, $\frac{\chi_{QS}}{T^2}$ have recently been calculated, at μ_B = 0, for a range of temperatures using lattice QCD simulations [B$^+$12]. The results are extrapolated to the continuum limit, thus can be directly compared to heavy-ion data for obtaining information on volume. For instance, for the particular case of most central $Au+Au$ collisions at $\sqrt{s_{NN}}$ = 200 GeV, the volume of the system can be calculated using the following equations:

$$V_{\chi_B} = \frac{144.57 \pm 13.21}{T^3(\chi_B/T^2)_{LQCD}} \tag{3.40}$$

$$V_{\chi_S} = \frac{200.195 \pm 17.96}{T^3(\chi_S/T^2)_{LQCD}} \tag{3.41}$$

$$V_{\chi_{QS}} = \frac{87.02 \pm 11.13}{T^3(\chi_{QS}/T^2)_{LQCD}} \tag{3.42}$$

The quantities $(\chi_{B,S,QS}/T^2)_{LQCD}$ represent the susceptibilities as obtained from lattice QCD simulations. Similar equations can be used for other centrality bins. Figures 3.7, 3.8(left) shows the variation of volume as a function of temperature determined from equations (3.37), (3.38), (3.39).

To summarize, we have calculated $\omega_{ch,dyn}$ & $\langle N_{ch}\rangle$ using NBD fits and the variation of volume with temperature using HIJING event generator and LQCD simulation results. Using equation (3.15) we can now determine the variation of isothermal compressibility (k_T) with temperature over the range 150 $\leq$ T $\leq$ 250 MeV for various centrality bins of $Au+Au$ collisions at $\sqrt{s_{NN}}$ = 200 GeV. Figure 3.8 (right) shows the variation of k_T with T for most central $Au+Au$ collisions at $\sqrt{s_{NN}}$ = 200 GeV using VvsT results from the three susceptibilities.

Table 3.2: Tabulation of the net baryon number, strangeness and strangeness-charge susceptibilities for $Au + Au$ collisions at $\sqrt{s_{NN}}$ = 200 GeV using HIJING event generator at midrapidity, -0.5 < y < 0.5 and over the transverse momentum range 0.2 < p_T < 2.0 GeV/c

Centrality	$VT^3\left(\frac{\chi_B}{T^2}\right)$	$VT^3\left(\frac{\chi_S}{T^2}\right)$	$VT^3\left(\frac{\chi_{QS}}{T^2}\right)$
0-5	144.57 ±13.21	200.195 ±17.96	87.02 ±11.13
5-10	115.094 ±11.82	167.95 ±16.11	70.292 ±10.05
10-15	92.82 ±10.59	135.704 ±14.50	57.10 ±9.05
15-20	74.94 ±9.52	109.94 ±13.14	46.32 ±8.21
20-25	60.76 ±8.60	89.2 ±11.77	37.83 ±7.43
25-30	48.65 ±7.67	71.83 ±10.48	30.48 ±6.54
30-35	49.89 ±7.75	73.53 ±10.66	31.14 ±6.69
35-40	30.72 ±6.07	45.77 ±8.40	19.35 ±5.24
40-45	24.25 ±5.39	36.33 ±7.51	15.32 ±4.66

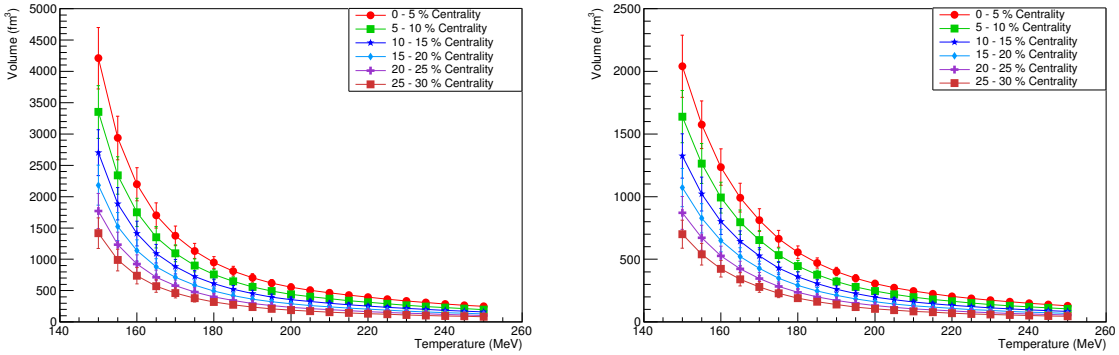

Figure 3.7: Volume as a function of temperature for various centralities of $Au + Au$ collisions at $\sqrt{s_{NN}}$ = 200 GeV calculated (Left) using equation (3.37) (Right) using equation (3.38)

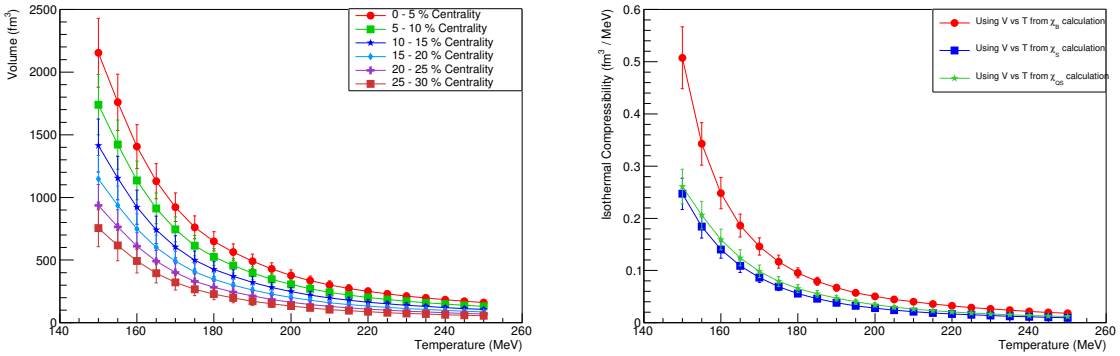

Figure 3.8: (Left) Volume as a function of temperature calculated from equation (3.39) for various centralities of $Au + Au$ collisions at $\sqrt{s_{NN}}$ = 200 GeV (Right) Variation of k_T with T for most central $Au + Au$ collisions at $\sqrt{s_{NN}}$ = 200 GeV using VvsT results from the three susceptibilities.

Chapter 4

Transverse Momentum Distribution

4.1 Introduction

The main objective of heavy-ion collisions is to analyse the properties of the hot and dense matter (QGP) produced in these collisions. QGP, however, is a transient state, existing for a very short time, thus making it extremely difficult to use external probes to study its properties which must rather be inferred from the impact left by the plasma on the particles flying out of the collision region. The study of transverse momentum (p_t) distribution of the identified particles has been proved to be a promising tool for this purpose.

In the present work, we have employed several models to obtain the best approximation to the experimental data on transverse momentum distribution (p_t) of identified particles from $Pb + Pb$ collisions at $\sqrt{s_{NN}}$ = 2.76 TeV for various centrality classes. The terms longitudinal and transverse are defined with respect to the beam direction.

Before discussing these models in detail, let's try to answer a very fundamental question: ***why is the transverse momentum distribution so important?***

Inside the RHIC and LHC, two high-energy particle beams are accelerated to very high speeds before they are made to collide head-on. Before collision the beams have only a longitudinal momentum. However, after the collision the particles can be seen flying out of the collision region with a non-zero transverse momenta. Thus a study of p_t-distribution of the outgoing particles in the collision can give an insight into the physics involved in the collision process. In addition, the fact that the transverse momentum is Lorentz invariant for boosts along the beam direction is another mathematical advantage. Also, as pointed out in section 2.5.3, sometimes it is difficult to measure the longitudinal momenta of particles,

especially for high p_z particles, since the beam pipe can be in the way of estimating it.

4.2 Experimental result on p_t-distribution of negative pions produced in $Pb + Pb$ collision at $\sqrt{s_{NN}}$ = 2.76 TeV

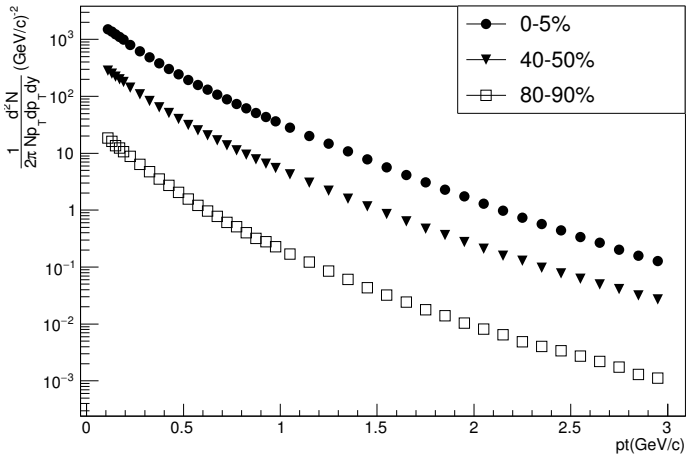

Figure 4.1: Transverse momentum distribution of negative pions produced in $Pb + Pb$ collisions at $\sqrt{s_{NN}}$ = 2.76 TeV for three centrality classes. (Data Source: [A$^+$13a])

Figure 4.1 shows the transverse momentum distribution of the π^- particles produced in $Pb + Pb$ collisions at $\sqrt{s_{NN}}$ = 2.76 TeV for three centrality classes. The x-axis is simply p_t in GeV/c. The y-axis represents the Lorentz Invariant Differential yield, E$\frac{d^3N}{d^3p}$.

To show that the quantity E$\frac{d^3N}{d^3p}$ represents the Lorentz Invariant Differential yield, we first need to prove that d^3p/E is lorentz invariant. Here we are talking about lorentz invariance for boosts along the beam direction. For Lorentz boost in longitudinal direction, we have

$$p_z^* = \gamma(p_z - \beta E) \tag{4.1}$$

Its differential is given by

$$\begin{aligned} dp_z^* = \gamma(dp_z - \beta dE) = \gamma(dp_z - \beta\frac{p_z dpz}{E}) \\ = \frac{dp_z}{E}\gamma(E - \beta p_z) = \frac{dp_z}{E}E^* \end{aligned} \tag{4.2}$$

where we have used $E^2 = m^2 + p_t^2 + p_z^2$. From this we get $EdE = p_z dp_z$. Thus the quantity dp_z/E is Lorentz invariant. Since p_t is Lorentz invariant, d^3p/E is also Lorentz invariant.

Now

$$E\frac{d^3N}{d^3p} = E\frac{d^3N}{d^2p_t dp_z} = \frac{d^3N}{d^2p_t dy} = \frac{d^3N}{2\pi p_t dp_t dy} \tag{4.3}$$

where the relation dp_z/E = dy is used. The data on the vertical axis has been normalized by the total number of events (N) considered.

Given below is a brief account of the models used for fitting the p_t-distribution shown in Figure 4.1 and their fitting results.

4.2.1 Boltzmann Distribution

In this model, we consider the production of particles in heavy-ion collisions as due to a thermal source at temperature T and thus we can describe the source of particle emission by a Boltzmann Distribution.

$$f_{BG} = Ae^{\frac{-p_T}{T}} \tag{4.4}$$

where A is some normalization factor. In the present case, the following form of Boltzmann distribution is used,

$$f_{BG} = \frac{V}{(2\pi)^3} m_T e^{\frac{-m_T}{T}} \tag{4.5}$$

where $m_T = \sqrt{m^2 + p_t^2}$ is the transverse mass and m is the rest mass of π^- particles. Figure 4.2 shows the result of Boltzmann fitting to the p_t-distribution shown in Figure 4.1. The fitting parameters for the Boltzmann fitting along with the $\frac{\chi^2}{NDF}$ values are listed in Table 4.1.

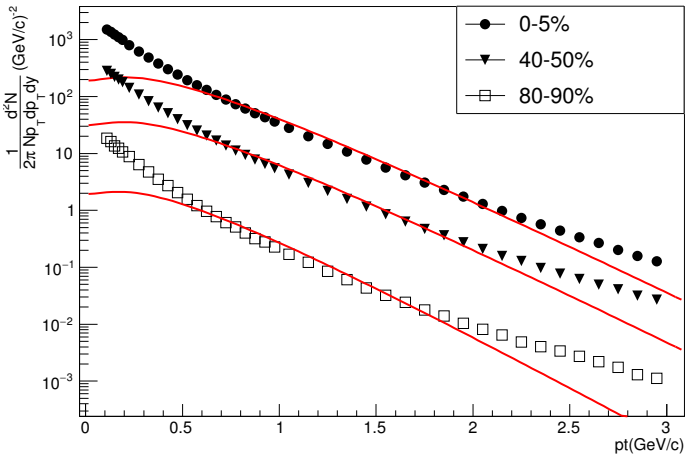

Figure 4.2: Transverse momentum distribution of π^- particles produced in $Pb + Pb$ collisions at $\sqrt{s_{NN}}$ = 2.76 TeV. The red lines shows the Boltzmann fitting.

Table 4.1: Result of Boltzmann fitting to the p_t-distribution shown in Figure 4.1

Centrality	Temperature (GeV)	$\frac{\chi^2}{NDF}$
0-5	0.246 $\pm$0.0016	954.983/39
40-50	0.241 $\pm$0.0018	1425/39
80-90	0.220 $\pm$0.0021	1807/39

As can be seen, the fitting is not at all good. It also tells us that merely considering the particle production in these collisions as due to a thermal source does not serve our purpose and that there are many other underlying physics phenomena that need to be considered. Two such phenomena are the *flow effect* and contribution of *resonance decays*. These are being taken into account in Boltzmann-Gibbs Blast Wave (BGBW) Model, as explained below.

4.2.2 Boltzmann-Gibbs Blast Wave Model

As we studied in the case of elliptic flow (section 2.4.1), the QGP produced in high energy heavy-ion collisions will expand against the outside vacuum due to thermodynamic pressure gradient. During the expansion, the multiple collisions among the constituent particles will translate the initial azimuthal anisotropy of the reaction zone into the momentum anisotropy of the produced particles. Thus evidently, the effect of flow needs to be taken into account while studying the momentum distribution of the particles produced in the collision.

Resonance Decays Contribution: In addition to thermally emitted pions, there are also pions which are produced from the decays of resonances, for e.g.,

$$\rho^0 \rightarrow \pi^+\pi^-, \omega \rightarrow \pi^+\pi^0\pi^-, \Delta \rightarrow N\pi^- \tag{4.6}$$

In experiments, these resonances are produced in abundant amounts. It has been found that the resonance decays contribution result in very sharply falling pion spectra and raise significantly the total pion production at low m_T/p_t [SSH93].

Boltzmann-Gibbs Blast Wave Model takes both the above mentioned contributions into account. Since we are dealing with the transverse momentum distribution, we only need to take into account the transverse flow of the thermalized medium (QGP) produced in heavy-ion collisions.

The Boltzmann-Gibbs Blast Wave function is given by [SSH93] :

$$f_{BGBW} = \frac{V m_T}{(2\pi)^3} \int_0^R r dr K_1\Big(\frac{m_T cosh\rho}{T}\Big) I_0\Big(\frac{p_t sinh\rho}{T}\Big) \tag{4.7}$$

where $\rho = tanh^{-1}(\beta_r)$ and β_r describes the velocity distribution, along the transverse direction, in the region $0 \leq$ r $\leq$ R.

$$\beta_r(r) = \beta s\Big(\frac{r}{R}\Big)^n \tag{4.8}$$

In the present analysis, n has been customarily put equal to 2. β_s is the surface velocity. Figure 4.3 shows the result of BGBW fitting to the p_t-distribution shown in Figure 4.1. The fitting parameters for this fitting along with the $\frac{\chi^2}{NDF}$ values are listed in Table 4.2.

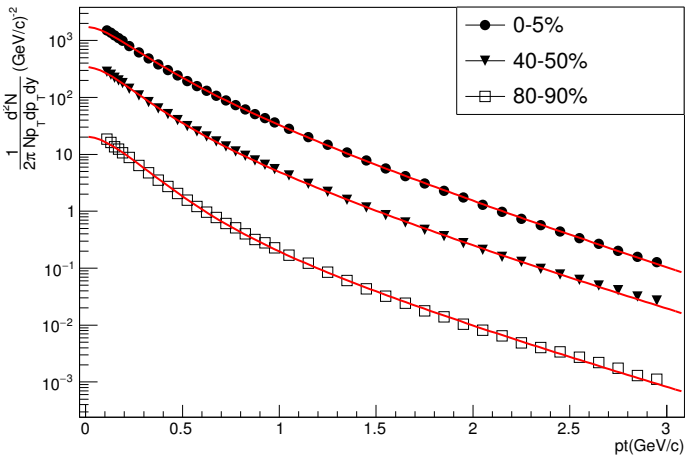

Figure 4.3: p_t-distribution of π^- particles produced in $Pb + Pb$ collisions at $\sqrt{s_{NN}}$ = 2.76 TeV. The red lines represent Boltzmann-Gibbs Blast Wave fitting.

As can be seen, the BGBW model describes the experimental data really well. Before turning our attention to the heat capacity calculation, we will consider one more model which has recently gained importance in high-energy physics with very good quality fits of p_t-distributions.

Table 4.2: Result of BGBW fitting to the p_t-distribution shown in Figure 4.1

Centrality	Temperature (GeV)	β_s	$\frac{\chi^2}{NDF}$
0-5	0.0745 $\pm$0.0279	0.947 $\pm$0.038	5.74/37
40-50	0.0827 $\pm$0.0469	0.945 $\pm$0.057	12.79/37
80-90	0.104 $\pm$0.0061	0.923 $\pm$0.0065	25.7/37

4.2.3 Tsallis-Boltzmann Model

In this model, the formalism of nonextensive statistical mechanics [Tsa09] has been used in characterizing the system produced in heavy-ion collisions. It is based on the extremization of the Tsallis entropies

$$S_q = \frac{k}{q-1}(1 - \sum\nolimits_i p_i^q) \tag{4.9}$$

The above equation is a generalization of the Boltzmann-Gibbs (BG) entropy. k is the Boltzmann constant. There is, however, no direct procedure for generalizing the BG theory. In literature, a metaphor has been used for for this purpose.

Consider the following differential equation

$$\frac{dy}{dx} = y^q \tag{4.10}$$

with the initial condition y(0)=1. It's solution is

$$y = (1 + (1-q)x)^{\frac{1}{1-q}} \tag{4.11}$$

In the limit q $\rightarrow$ 1 the above equation reduces to the ordinary exponential function, e^x. Thus equation (4.11) can be seen as a generalization of the ordinary exponential function.

$$y = (1 + (1-q)x)^{\frac{1}{1-q}} = e_q^x \tag{4.12}$$

where e_q^x is called the q-exponential. Figure 4.4 shows the variation of q-exponential with x for various values of q.

Similarly we can define q-logarithm as

$$y = \frac{x^{(1-q)} - 1}{1-q} = ln_q x \tag{4.13}$$

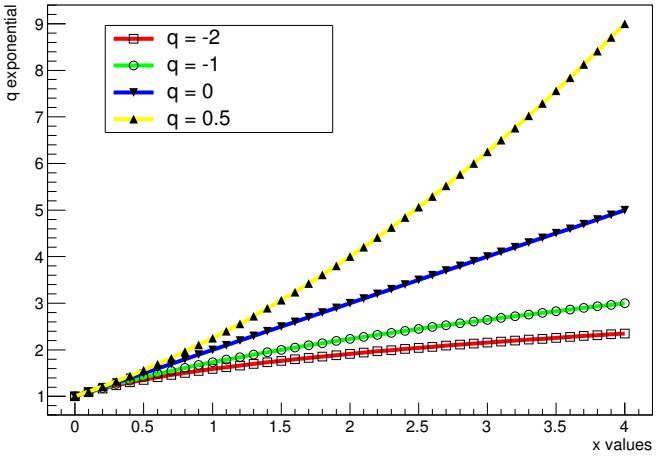

Figure 4.4: e_q^x as a function of x for various values of q

where $ln_q x = \ln x$ in the limit of q $\to 1$. It is easy to show that $ln_q x$ satisfies the following property

$$ln_q(x_A x_B) = ln_q(x_A) + ln_q(x_A) + (1-q) ln_q(x_A) ln_q(x_A) \tag{4.14}$$

The Boltzmann-Gibbs entropy is given by

$$S_{BG} = -k \sum_{i=1}^{W} p_i ln p_i \tag{4.15}$$

with the property

$$\sum_{i=1}^{W} p_i = 1 \tag{4.16}$$

where W represents the total number of microstates and p_i is the probability of finding the system in the i^{th} microstate. Using equation (4.13) we can define the q-generalization of the BG entropy as

$$\begin{aligned} S_q = -k \sum_{i=1}^{W} p_i ln_q p_i &= k \sum_{i=1}^{W} p_i ln_q(1/p_i) \\ &= k \sum_{i=1}^{W} p_i \frac{(1/p_i)^{(1-q)} - 1}{1-q} \\ &= \frac{k}{q-1} \sum_{i=1}^{W} p_i \Big(1 - (\frac{1}{p_i})^{1-q}\Big) \\ &= \frac{k}{q-1} \Big(\sum_{i=1}^{W} p_i - \sum_{i=1}^{W} p_i^q \Big) \end{aligned} \tag{4.17}$$

Finally using equation (4.16) we obtain

$$S_q = \frac{k}{q-1} \big(1 - \sum\nolimits_i p_i^q\big) \tag{4.18}$$

An important property of this q-entropy is it's non-additive nature.

$$\frac{S_q(A+B)}{k} = \frac{S_q(A)}{k} + \frac{S_q(B)}{k} + (1-q)\frac{S_q(A)}{k}\frac{S_q(B)}{k} \tag{4.19}$$

with A and B being two independent subsystems, i.e. the joint probability satisfies p_{ij}^{A+B} = $p_i^A p_j^B$ for all i and j, of one whole system. Thus Tsallis entropies are nonextensive in nature.

In the present work the ordinary exponential in equation (4.5) is replaced with q-exp.

$$\frac{V}{(2\pi)^3} m_T e^{\frac{-m_T}{T}} \rightarrow \frac{V}{(2\pi)^3} m_T e_q^{\frac{-m_T}{T}} \tag{4.20}$$

so that the Tsallis-Boltzmann function is given by [CW12]

$$f_{TB} = \frac{V}{(2\pi)^3} m_T \Big(1 + \frac{(1-q)m_T}{T}\Big)^{\frac{1}{1-q}} \tag{4.21}$$

Figure 4.5 shows the result of fitting the transverse momentum distribution of negative pions produced in $Pb + Pb$ collisions by equation (4.21) for two different p_t ranges. The fitting parameters for Tsallis-Boltzmann fitting along with the $\frac{\chi^2}{NDF}$ values are listed in Table 4.3.

As can be seen the Tsallis-Boltzmann model gives a good approximation to the experimental data. The fitting is relatively good over $0.2 < p_t < 3.0$ GeV/c.

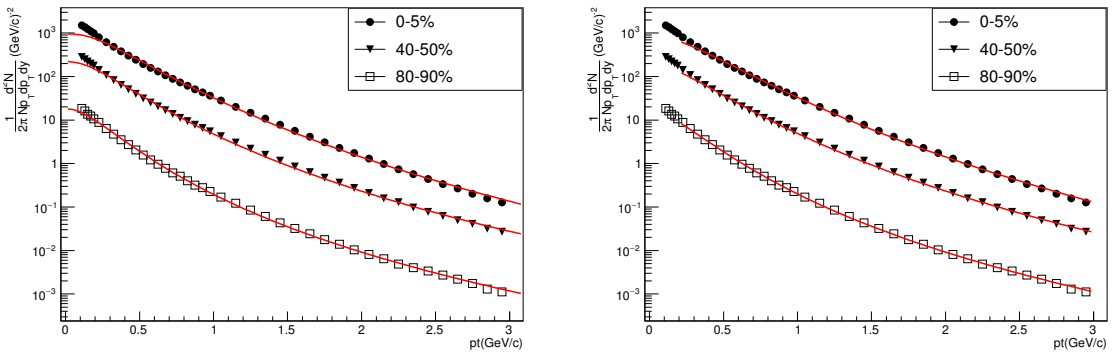

Figure 4.5: Transverse momentum distribution of π^- particles produced in $Pb + Pb$ collisions at $\sqrt{s_{NN}}$ = 2.76 TeV fitted with Tsallis-Boltzmann function for $0 < p_t < 3.0$ GeV/c (Left) and $0.2 < p_t < 3.0$ GeV/c (Right)

Table 4.3: Result of Tsallis-Boltzmann fitting to the p_t-distribution shown in Figure 4.1

Centrality	Temperature (GeV)	q	$\frac{\chi^2}{NDF}$ for Fig. 4.5 Left	$\frac{\chi^2}{NDF}$ for Fig. 4.5 Right
0-5	0.1296 $\pm$0.0037	1.11 $\pm$0.0033	86.65/38	45.55/33
40-50	0.1072 $\pm$0.0031	1.13 $\pm$0.030	70.04/38	31.12/33
80-90	0.0803 $\pm$0.0029	1.15 $\pm$0.0028	32.82/38	14.94/33

A comparison of the three models has been given in the next section. But before moving to that, there are two important questions that need to be answered.

- What is the physical significance of the Tsallis parameter q?
- Why the nonextensive statistical mechanics approximates well the experimental data, i.e. what is the source of nonextensivity in our system?

It has been shown that the non-extensivity parameter q is related to the fluctuations of temperature in the system [Bec02].
For the distribution function given by

$$f(x) = [1 + (q-1)\frac{x}{\lambda}]^{\frac{q}{q-1}} \tag{4.22}$$

It can be shown that

$$\omega = \frac{\langle(\frac{1}{\lambda})^2\rangle - \langle\frac{1}{\lambda}\rangle^2}{\langle\frac{1}{\lambda}\rangle^2} = q - 1 \tag{4.23}$$

In case of p_t distribution, the quantity λ is Temperature T. Thus the Tsallis parameter q is related to the fluctuations of temperature in the system. The existence of temperature fluctuations is an experimentally observed fact. For instance, Figure 4.6 shows the temperature distribution of 10,000 HIJING events for most central $Pb + Pb$ collisions at $\sqrt{s_{NN}}$ = 2.76 TeV.

The laws of Statistical Mechanics are generally applicable to a system comprising of a huge number of particles, of the order of Avogadro's number. However, in the present case of high-energy heavy-ion collisions, there are only some thousands of particles being produced in the final state and yet Tsallis statistics gives a very good approximation to the experimental results. It seems that the additional parameter q is taking care of that. And

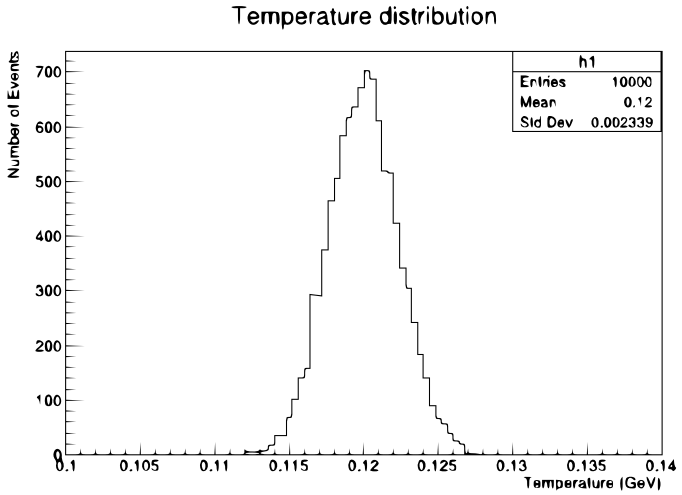

Figure 4.6: Temperature distribution for 10,000 HIJING events of most central $Pb + Pb$ collisions at $\sqrt{s_{NN}}$ = 2.76 TeV

this is why the nonextensivity is coming into picture i.e. we are applying a statistical model to a system comprised of a very small number of particles.

4.3 Comparison of the three models

From the fitting results, shown in Tables 4.1, 4.2 and 4.3, we can conclude that Boltzmann Model alone cannot describe well the experimental data unless some other contributions are taken into account which leads us to the Boltzmann-Gibbs Blast Wave Model. A very important thing to note here is, whether a model provides a good approximation to the experimental data or not depends not only on the χ^2/NDF value but also on the physics involved. Although the BGBW model fits the experimental data with very low χ^2/NDF values but it does not take into account a very important property of nonextensivity. This is the reason why Tsallis model is regarded as the best approximation to the experimental results till date. We can still go further and define Tsallis Blast Wave Model [TXR+09]. However, the model is too complex and outside the scope of this thesis.

Chapter 5

Determination of Heat Capacity

5.1 Introduction and Methodology

The heat capacity, C_v, is the quantity of heat needed to raise the temperature of a system by one unit of temperature at a constant volume.

$$C_v = \frac{dE}{dT} \tag{5.1}$$

where the symbols have their usual meanings. The specific heat, c_v, is obtained by dividing the heat capacity by the total number of particles in the system.

The heat capacity of a system can be related to the fluctuations of temperature in the system as [LL]

$$\frac{1}{C_v} = \frac{\langle T^2 \rangle - \langle T \rangle^2}{\langle T \rangle^2} \tag{5.2}$$

Thus the heat capacity of the hadronic matter formed in heavy-ion collisions can be determined by considering the event-by-event fluctuations of temperature.

The temperature parameter can be obtained by fitting the p_t-distribution of the identified particles in the collision. In the present analysis, we have made use of the fact that at low p_t, the transverse momentum distribution is described well by the Boltzmann distribution. The following procedure is used for heat capacity determination: First, 1,00,000 HIJING events are generated for most central $Pb + Pb$ collisions at $\sqrt{s_{NN}}$ = 2.76 TeV. For each event, the multiplicity weighted p_t-distribution for charged pions,

$$P(p_t) = \frac{M_{\pi^+}}{M_{\pi^+} + M_{\pi^-}} P(p_t)_{\pi^+} + \frac{M_{\pi^-}}{M_{\pi^+} + M_{\pi^-}} P(p_t)_{\pi^-} \tag{5.3}$$

is fitted to an exponential distribution

$$P(p_t) = Ae^{\frac{-p_t}{T}} \tag{5.4}$$

over the p_t range, $0.2 < p_t < 0.8$ GeV/c, to extract the temperature parameter. A is some normalization factor. Once the heat capacity is calculated, the specific heat can be determined by dividing the heat capacity with the factor $\langle M \rangle$ defined as

$$\langle M \rangle = \frac{\langle M_{\pi^+} \rangle}{\langle M_{\pi^+} \rangle + \langle M_{\pi^-} \rangle} \langle M_{\pi^+} \rangle + \frac{\langle M_{\pi^-} \rangle}{\langle M_{\pi^+} \rangle + \langle M_{\pi^-} \rangle} \langle M_{\pi^-} \rangle \tag{5.5}$$

where M represents multiplicity and $\langle .. \rangle$ defines average over events.

5.2 Simulation Results

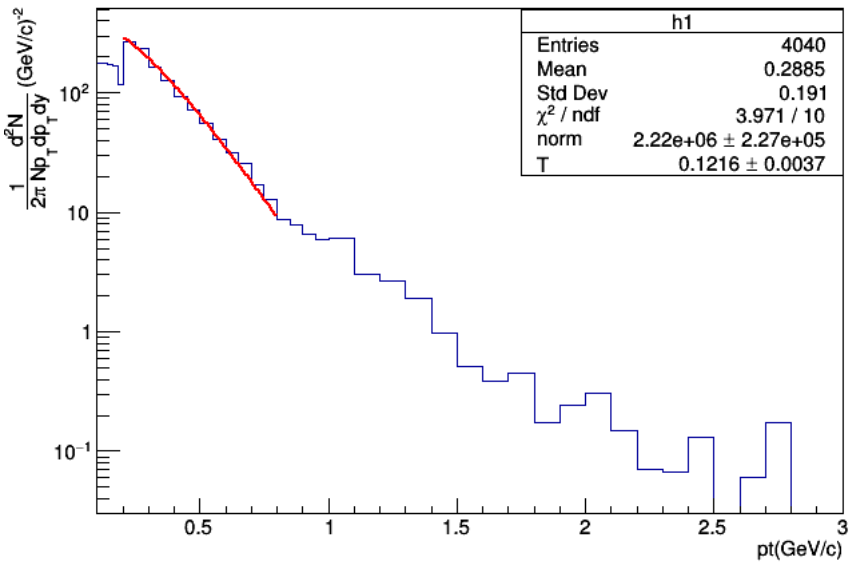

Figure 5.1: p_t-distribution for a single HIJING event of most central $Pb + Pb$ collision fitted to an exponential function over the range $0.2 < p_t < 0.8$ GeV/c.

Figure 5.1 shows the p_t-distribution for a single HIJING event of most central $Pb + Pb$ collision fitted to an exponential function over the range $0.2 < p_t < 0.8$ GeV/c. Our calculation yields the value for heat capacity and $< M >$ to be 1326.73 $\pm$ 70.97 and 1202.7 $\pm$ 116.673 respectively so that the value of specific heat per pion turns out to be 1.103 $\pm$ 0.122.

5.3 Another Method

The method outlined above is from [SLH+07]. In this section a novel method has been proposed for the specific heat calculation.

The proposed method is based on using the transverse momentum distribution data for two different centralities of $Pb + Pb$ collisions at $\sqrt{s_{NN}}$ = 2.76 TeV. Fitting these data to Tsallis-Boltzmann model will yield two different temperature values. Now if somehow, we can obtain information on the initial energy of the system at these two different temperatures, then the direct application of equation (5.1) will lead us to the heat capacity of the system.

There is, however, no direct approach of finding the total energy of the system in a given centrality class. An indirect approach has been used which is based on some representative results of lattice QCD simulations. Several groups around the world are involved in such simulations. In the following, the lattice QCD simulation results on $\frac{\epsilon}{T^4}$ (ϵ is the energy density) as a function of temperature (T in MeV) are from Wuppertal-Budapest Collaboration [BEF+10].

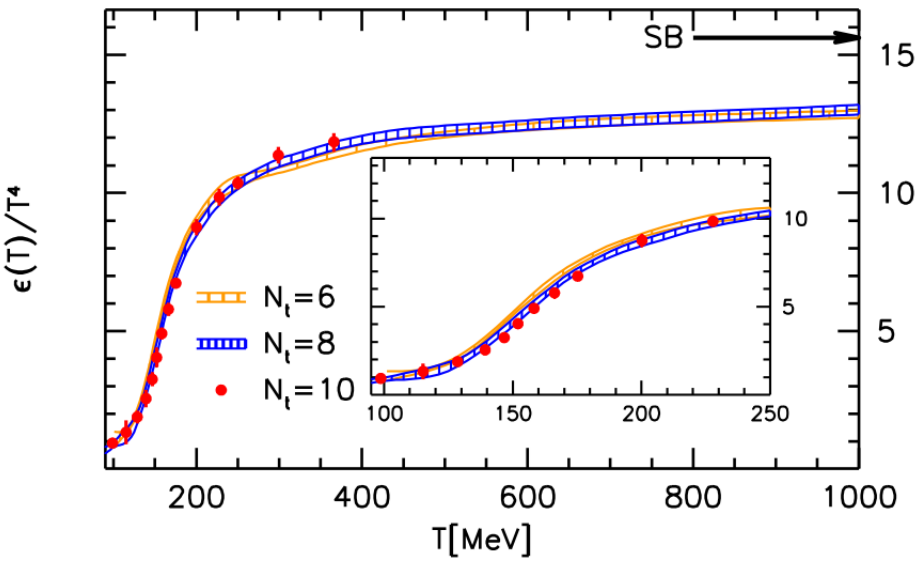

Figure 5.2: Lattice QCD simulations for $\frac{\epsilon}{T^4}$ as a function of T (in MeV) (Image source: [BEF+10])

Once we know the energy density of the system at a given temperature, we only need information on the volume of the system corresponding to that temperature and the method

for calculating the volume has already been discussed in section 3.3.1.

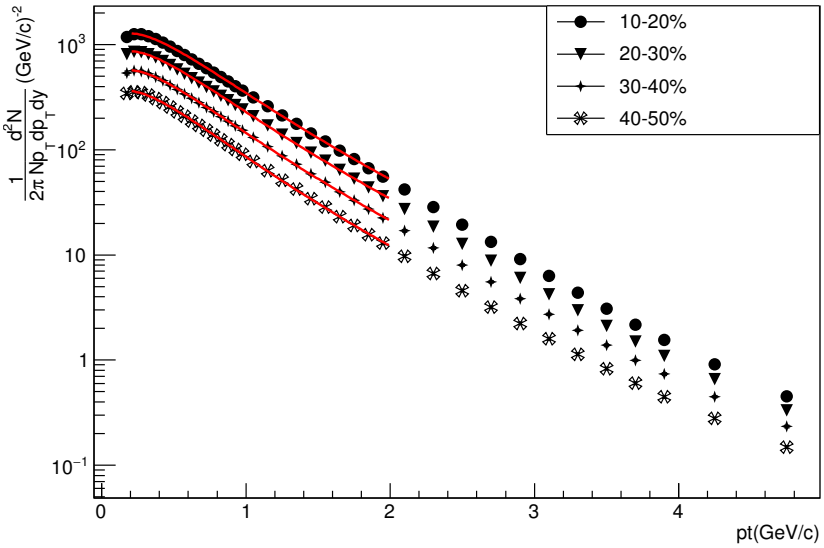

Figure 5.3: p_t-distribution of primary charged particles in the η range -0.8 $< \eta <$ 0.8 for various centrality classes of $Pb + Pb$ collisions at $\sqrt{s_{NN}}$ = 2.76 TeV . The red lines are the Tsallis-Boltzmann fits over the range 0.2 $< p_t <$ 2.0 GeV/c. (Data source: [A$^+$18])

Table 5.1: Data extracted from Figure (5.2) for $\frac{\epsilon}{T^4}$ as a function of T (in MeV)

Temperature (MeV)	$\frac{\epsilon}{T^4}$
98.957	0.926
115.190	1.316
128.727	1.885
139.025	2.551
147.162	3.250
152.601	4.046
158.582	4.908

Temperature (MeV)	$\frac{\epsilon}{T^4}$
166.727	5.785
175.955	6.728
227.978	9.864
200.365	8.775
250.161	10.368
299.933	11.391
366.439	11.863

Table 5.2: Tabulation of the various quantities required for the calculation of heat capacity. The first column lists the temperature values obtained from the Tsallis-Boltzmann fits shown in Fig. (5.3). The quantities in the remaining columns are obtained from the cubic spline interpolation method.

Centrality	Temperature (MeV)	$\frac{\epsilon}{T^4}$	$\left(\frac{\chi_B}{T^2}\right)_{LQCD}$	$\left(\frac{\chi_S}{T^2}\right)_{LQCD}$	$\left(\frac{\chi_{QS}}{T^2}\right)_{LQCD}$
10-20	236.214	10.061	0.27926	0.77809	0.26332
20-30	232.853	10.007	0.27690	0.77234	0.26190
30-40	227.194	9.8437	0.27289	0.76143	0.25903
40-50	219.714	9.6337	0.26738	0.74297	0.25344

Figure 5.3 shows the p_t-distribution of the primary charged particles in the η range -0.8 $< \eta <$ 0.8 for various centrality classes of $Pb+Pb$ collisions at $\sqrt{s_{NN}}$ = 2.76 TeV overlaid with fits to Tsallis-Boltzmann distribution. The temperature parameters listed in Table 5.2 are the results of these fits. Using Table V from [B$^+$12] for the continuum extrapolated values of $\left(\frac{\chi_{B,S,QS}}{T^2}\right)_{LQCD}$ and the cubic spline interpolation method, we obtain the values listed in columns 4, 5 and 6 of Table 5.2 for the net baryon number, strangeness and strangeness-charge correlation susceptibilities. Similarly, Table 5.1 have been used together with cubic spline interpolation method to extract the values listed in column 3 of Table 5.2 for energy density.

Using the information presented in Tables 5.2 and 5.3, we can calculate the energy available to a single particle (E) for a particular centrality class, Table 5.4. Note that in all the calculations only the central values of all the quantities involved are used. We have data corresponding to four centrality classes and thus we can have six combinations. Table 5.5 shows the values of specific heat as obtained from the values of E_B, E_S and E_{QS} shown in Table 5.4. Figure 5.4 is a graphical depiction of Table 5.5.

It can be seen that the values of specific heat listed in columns 3 and 4 (c_s and c_{QS}) of Table 5.5 are quite consistent with each other. However, the specific heat estimates obtained using volume information from net baryon number susceptibility (c_B) are very different from the other two estimates (c_s and c_{QS}).

Table 5.3: Tabulation of the strangeness, net baryon number and strangeness-charge susceptibilities for various centrality classes of $Pb + Pb$ collisions at $\sqrt{s_{NN}}$ = 2.76 TeV using HIJING event generator for -0.8 $< \eta <$ 0.8 and over the range 0.2 $< p_t <$2.0 GeV/c in four centrality classes. $N_{charged}$ represents the total charged particle number in the given pseudorapidity and p_t range.

Centrality	$VT^3\left(\frac{\chi_S}{T^2}\right)$	$VT^3\left(\frac{\chi_B}{T^2}\right)$	$VT^3\left(\frac{\chi_{QS}}{T^2}\right)$	$N_{charged}$
10-20	598.101 $\pm$50.067	342.483 $\pm$29.008	259.035 $\pm$34.351	2635
20-30	387.482 $\pm$38.306	219.667 $\pm$23.331	168.138 $\pm$25.666	1709
30-40	245.213 $\pm$30.546	137.259 $\pm$17.730	107.062 $\pm$20.792	1075
40-50	145.663 $\pm$22.806	81.744 $\pm$13.378	63.480 $\pm$15.507	641

Table 5.4: Tabulation of energy available per particle corresponding to each centrality class using the information presented in the Tables (5.1 - 5.3) . $E_{B,S,QS}$ represents the values of energy per particle using $V_{B,S,QS}$ respectively.

Centrality	Temperature (MeV)	E_B (MeV)	E_S (MeV)	E_{QS} (MeV)
10-20	236.214	1106.105	693.283	887.239
20-30	232.853	1081.647	684.048	875.335
30-40	227.194	1046.405	669.978	859.869
40-50	219.714	1009.531	647.397	827.093

Table 5.5: Shown are the values of specific heat. $C_{B,S,QS}$ represents the values of specific heat calculated using $E_{B,S,QS}$ respectively.

S. No.	Combination	c_B	c_S	c_{QS}
1	10-20 and 20-30	7.28	2.75	3.54
2	10-20 and 30-40	6.62	2.58	3.03
3	10-20 and 40-50	5.85	2.78	3.65
4	20-30 and 30-40	6.23	2.49	2.73
5	20-30 and 40-50	5.49	2.79	3.67
6	30-40 and 40-50	4.93	3.02	4.38

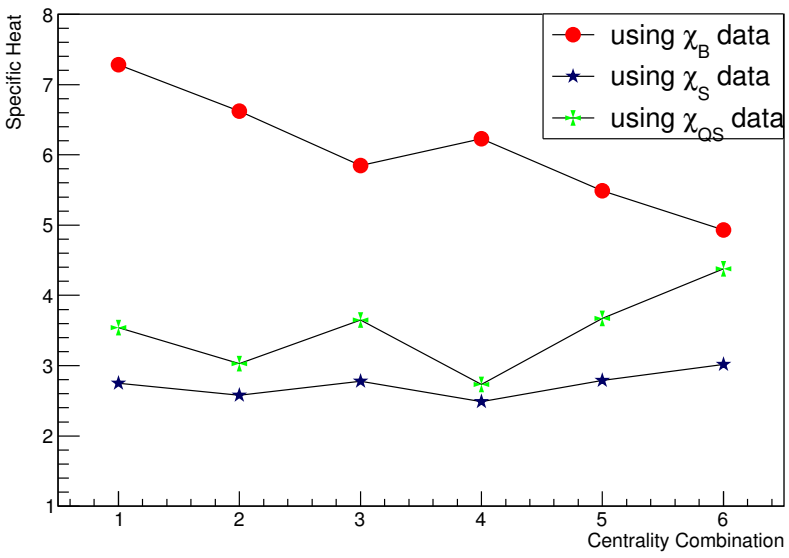

Figure 5.4: Graphical representation of the specific heat values listed in Table 5.5

Chapter 6

Summary

We have studied the isothermal compressibility and specific heat of the system formed in $Au+Au$ collisions at $\sqrt{s_{NN}}$ = 0.2 TeV and $Pb+Pb$ collisions at $\sqrt{s_{NN}}$ = 2.76 TeV respectively. We have shown the variation of k_T over a temperature range of 150 $\leq$ T $\leq$ 250 MeV using the volume information from net baryon number, strangeness and strangeness-charge correlation susceptibilities. However, it is not yet clear as to why the volume estimate calculated from net baryon number susceptibility is twice of that obtained from the other two susceptibilities, which is to be explored further. Multiplicity fluctuations have been obtained from available experimental data and HIJING event generator. We have seen that k_T decreases with increasing temperature. The estimation of k_T presented in this analysis depends on several assumptions, most importantly on the estimation of dynamical fluctuations. We have also calculated the specific heat using two different methods. The value of specific heat obtained from the proposed method is an order of magnitude different from that obtained in section 5.2. This is due to the fact that in one case pion spectra has been used to extract the temperature parameter from fitting the spectra to Boltzmann distribution whereas in the other case Tsallis-B model is being used to fit the p_t-distribution of primary charged particles to extract the temperature i.e. the basic starting points in the two cases are different. Thus it would be meaningless to talk of any comparison between these two values. The inspiration for this analysis is to search for the presence of an anticipated critical point in the QCD phase diagram. At the centre of mass energies considered, there is no proof of a critical behaviour with respect to the compressibility and specific heat observables. Although our study does not provide any indication of such behaviour, it does not mean that there is no critical point. We can calculate these quantities for different centre of

mass energies i.e. we can run a beam energy scan to look for any singularities. However, it has been shown in [A$^+$08] that there is no such evidence of a critical behaviour with respect to the isothermal compressibility over centre of mass energies from 22.5 to 200 GeV. Further measurements with the High Luminosity Large Hadron Collider will be possible during the coming years, allowing a more comprehensive search for critical behaviour.

Appendix A

Classical Ideal gas in a Grand Canonical Ensemble

For a classical ideal gas in 3D, the partition function for a single particle is given by

$$Z = \frac{1}{(2\pi\hbar)^3} \int d^3q \int d^3p e^{-\beta H} \tag{A.1}$$

where (q,p) are the coordinates of the particle in phase space. The hamiltonian H is given by

$$H = \sum_i \frac{p_i^2}{2m} \tag{A.2}$$

$$Z = \frac{1}{(2\pi\hbar)^3} \int d^3q \int d^3p e^{-\beta p^2/2m} \tag{A.3}$$

$$Z = \frac{1}{(2\pi\hbar)^3} \int d^3q \int d^3p e^{-\beta p^2/2m} = \frac{V}{(2\pi\hbar)^3} \int_0^\infty 4\pi p^2 e^{-\beta p^2/2m} dp \tag{A.4}$$

Solving this integral and simplifying the expression, we get

$$Z = V \left(\frac{m k_B T}{2\pi\hbar^2} \right)^{3/2} \tag{A.5}$$

The N particle partition function is

$$q = \frac{1}{N!} Z^N \tag{A.6}$$

The factor of $\frac{1}{N!}$ accounts for the indistinguishability of the particles.

The corresponding grand canonical partition function is defined as

$$Q = \sum_N e^{\beta \mu N} q \tag{A.7}$$

where μ is the chemical potential of the system.

$$Q = \sum_N e^{\beta\mu N} \frac{1}{N!} Z^N \tag{A.8}$$

This can be further simplified as

$$Q = \sum_N e^{\beta\mu N} \frac{1}{N!} Z^N = exp(Ze^{\beta\mu}) \tag{A.9}$$

Once we have the partition function, we can define the average number of particles as

$$\langle N \rangle = \frac{1}{\beta Q} \frac{\partial Q}{\partial \mu} = \frac{1}{\beta Q} (Q\beta Z e^{\beta\mu}) = Z e^{\beta\mu} \tag{A.10}$$

Now, using equation (3.13) and (A.10)

$$\langle N^2 \rangle - \langle N \rangle^2 = k_B T \Big(\frac{\partial \langle N \rangle}{\partial \mu} \Big) = Z e^{\beta\mu} = \langle N \rangle \tag{A.11}$$

Bibliography

[A+08] A. Adare et al., *Charged hadron multiplicity fluctuations in Au+Au and Cu+Cu collisions from* $\sqrt{s_{NN}} = 22.5$ *to 200 GeV*, Phys. Rev. **C78** (2008), 044902.

[A+13a] Betty Abelev et al., *Centrality dependence of* π*, K, p production in Pb-Pb collisions at* $\sqrt{s_{NN}}$ *= 2.76 TeV*, Phys. Rev. **C88** (2013), 044910.

[A+13b] ———, *Centrality determination of Pb-Pb collisions at* $\sqrt{s_{NN}}$ *= 2.76 TeV with ALICE*, Phys. Rev. **C88** (2013), no. 4, 044909.

[A+18] S. Acharya et al., *Transverse momentum spectra and nuclear modification factors of charged particles in pp, p-Pb and Pb-Pb collisions at the LHC*, JHEP **11** (2018), 013.

[Aea95] T. Abbott et al., *Multiplicity distributions from central collisions of O-16+Cu at 14.6A GeV/c and intermittency*, Phys. Rev. C **52** (1995), 58.

[B+93] J. Bächler et al., *Multiplicity distributions in small phase space domains in central nucleus-nucleus collisions*, Z. Phys. **C57** (1993), 541–550.

[B+12] A. Bazavov et al., *Fluctuations and Correlations of net baryon number, electric charge, and strangeness: A comparison of lattice QCD results with the hadron resonance gas model*, Phys. Rev. **D86** (2012), 034509.

[Bec02] Christian Beck, *Non-additivity of Tsallis entropies and fluctuations of temperature*, 5.

[BEF+10] Szabolcs Borsanyi, Gergely Endrodi, Zoltan Fodor, Antal Jakovac, Sandor D. Katz, Stefan Krieg, Claudia Ratti, and Kalman K. Szabo, *The QCD equation of state with dynamical quarks*, JHEP **11** (2010), 077.

[BMKRS15] Peter Braun-Munzinger, Alexander Kalweit, Krzysztof Redlich, and Johanna Stachel, *Confronting fluctuations of conserved charges in central nuclear collisions at the LHC with predictions from Lattice QCD*, Phys. Lett. **B747** (2015), 292–298.

[Cha14] A. K. Chaudhuri, *A short course on Relativistic Heavy Ion Collisions*, IOPP, 2014.

[CW12] J. Cleymans and D. Worku, *The Tsallis Distribution in Proton-Proton Collisions at $\sqrt{s}$ = 0.9 TeV at the LHC*, J. Phys. **G39** (2012), 025006.

[HM08] Francis Halzen and Alan D. Martin, *Quarks and leptons - an introductory course in modern particle physics*, Wiley, 2008.

[LKd18] Constantin Loizides, Jason Kamin, and David d'Enterria, *Improved Monte Carlo Glauber predictions at present and future nuclear colliders*, Phys. Rev. **C97** (2018), no. 5, 054910, [erratum: Phys. Rev.C99,no.1,019901(2019)].

[LL] L.D. Landau and E.M. Lifschitz, *Course of theoretical physics: Vol. 5, statistical physics (pergamon press, london- paris, 1958).*

[O$^+$14] K. A. Olive et al., *Review of Particle Physics*, Chin. Phys. **C38** (2014), 090001.

[SLH$^+$07] Ben-Hao Sa, Xiao-Mei Li, Shou-Yang Hu, Shou-Ping Li, Jing Feng, and Dai-Mei Zhou, *Specific heat in hadronic matter and in quark-gluon matter*, Phys. Rev. **C75** (2007), 054912.

[SSH93] Ekkard Schnedermann, Josef Sollfrank, and Ulrich W. Heinz, *Thermal phenomenology of hadrons from 200-A/GeV S+S collisions*, Phys. Rev. **C48** (1993), 2462–2475.

[Ste06] M. A. Stephanov, *QCD phase diagram: An Overview*, PoS **LAT2006** (2006), 024.

[Tsa09] Constantino Tsallis, *Introduction to nonextensive statistical mechanics*, Springer, 2009.

[TXR+09] Zebo Tang, Yichun Xu, Lijuan Ruan, Gene van Buren, Fuqiang Wang, and Zhangbu Xu, *Spectra and radial flow at RHIC with Tsallis statistics in a Blast-Wave description*, Phys. Rev. **C79** (2009), 051901.

[WG91] Xin-Nian Wang and Miklos Gyulassy, *hijing: A Monte Carlo model for multiple jet production in pp, pA, and AA collisions*, Phys. Review **D44, 3501** (1991).